

Characterization of local energy transfer in large-scale intermittent stratified geophysical flows via space filtering

Raffaello Foldes*

*CNRS, Ecole Centrale de Lyon, INSA Lyon, Université Claude Bernard Lyon 1,
Laboratoire de Mécanique des Fluides et d'Acoustique, UMR5509, F-69134 Ecully, France and
Dipartimento di Scienze Fisiche e Chimiche, Università dell'Aquila, L'Aquila, Italy*

Raffaele Marino

*CNRS, Ecole Centrale de Lyon, INSA Lyon, Université Claude Bernard Lyon 1,
Laboratoire de Mécanique des Fluides et d'Acoustique, UMR5509, F-69134 Ecully, France.*

Silvio Sergio Cerri

*Université Côte d'Azur, Observatoire de la Côte d'Azur, CNRS,
Laboratoire Lagrange, Bd de l'Observatoire, CS 34229, 06304 Nice cedex 4, France*

Enrico Camporeale

*School of Physical and Chemical Sciences, Queen Mary University of London, London E1 4NS, UK and
Space Weather Technology, Research and Education Center (SWx-TREC),
University of Colorado, Boulder, Colorado 80309, USA*

(Dated: December 5, 2024)

Recent studies based on simulations of the Boussinesq equations indicate that stratified turbulent flows can develop large-scale intermittency in the velocity and temperature fields, as detected in the atmosphere and in the oceans. In particular, emerging powerful vertical drafts were found to generate local turbulence, proving necessary for stratified flows to dissipate the energy as efficiently as homogeneous isotropic turbulent flows. The existence of regions characterized by enhanced turbulence and dissipation, as observed, for instance, in the ocean, requires appropriate tools to assess how energy is transferred across the scales and at the same time locally in the physical space. After refining a classical space-filtering procedure, here we investigate the feedback of extreme vertical velocity drafts on energy transfer and exchanges in subdomains of simulations of stably stratified flows of geophysical interest. Our analysis shows that vertical drafts are indeed able to trigger upscale and downscale energy transfers, strengthening the coupling between kinetic and potential energies at certain scales, depending on the intensity of the local vertical velocity.

I. INTRODUCTION

Stratified turbulence is widely investigated in the context of weather and climate studies. Indeed, the atmosphere and oceans are rotating and stratified flows, with their dynamics strongly influenced by the propagation of inertio-gravity waves from synoptic ($\sim 10^3$ km) to mesoscale ($\sim 10^2$ km). At the sub-mesoscale (~ 10 km) motions are much less controlled by force balances, and the interplay between turbulent fluctuations and propagating internal waves makes geophysical flows significantly different from homogeneous isotropic turbulence (HIT), even considering their dry dynamics only [1, 2]. Rotation and anisotropy do affect the way energy is transferred in Fourier space [3], allowing for the onset of an inverse energy cascade [4, 5], which was found to occur simultaneously to a direct energy cascade in geophysical fluids [2, 6–8]. In the presence of stratification, the potential temperature is coupled with the velocity field, opening a channel for the exchange between kinetic and potential energy modes [9]. A measure

of the strength of gravity waves in stratified turbulent flows is provided by the Froude number, $Fr = \tau_{W_g}/\tau_{NL}$, defined as the ratio between the characteristic time associated to buoyancy (N), $\tau_{W_g} = 1/N$, and the nonlinear time $\tau_{NL} = L_{int}/U_{rms}$, where L_{int} and U_{rms} represent the integral scale and the characteristic root mean square (RMS) velocity of the system, respectively. Using direct numerical simulations (DNS), it has been shown that both vertical velocity and potential temperature in stratified turbulent flows can exhibit large-scale intermittent statistics [10, 11], departing from Gaussian distributions, developing extreme field fluctuations as observed in the atmospheric boundary layer [12, 13], stratosphere [14], mesosphere [15], and oceans [16]. The concept of intermittency in turbulence is broad, with intermittent phenomena being observed in a variety of frameworks in nature, on Earth, as just mentioned, and in the outer space [17, 18]. Generally associated with the departure of the small-scale field fluctuations statistics from gaussianity, it can indeed occur as well at large scales [19]. Extensive parametric explorations presented in [11, 20] using DNS of the Boussinesq equations, demonstrated that powerful large-scale vertical drafts and temperature bursts occur in a certain range of Froude numbers of

* raffaello.foldes@ec-lyon.fr

geophysical interest. These authors also proposed simplified models explaining how extreme events arise from resonant interactions between internal gravity waves and turbulent motions [10, 21–23]. The causal link between the emergence of extreme vertical velocity drafts, the fourth-order moment of the vertical velocity (namely, the kurtosis K_w), and the enhancement of local turbulence, dissipation and mixing in stratified flows was also established [11, 23–25]. In particular, vertical drafts proved to be essential for stratified turbulent flows to dissipate energy as efficiently as HIT flows [23], providing an explanation for the relation observed in the ocean between the intermittent emergence of localized turbulence pattern and the dissipation being concentrated in a relatively small portion of the global ocean volume [26, 27]. While the contribution of extreme vertical velocity drafts to the energetics of stratified turbulent flows has been so far assessed in terms of their feedback on the domain volume statistics, their irregular emergence in space and time makes it difficult to investigate how these affect the spectral energy distribution at the location where they are detected. Classical three-dimensional Fourier transforms are in fact global operations, implying overall volume computations, thus averaging over regions whose dynamics can vary significantly for the presence of large-scale intermittent events. In order to investigate kinetic and potential energy transfers across scales in regions characterized by large values of the vertical velocity, we apply the well-known space-filtering, or coarse-graining, approach [28–30] to three-dimensional DNS of the Boussinesq equations. We refine the implementation of spatial filters to obtain accurate estimates of the axisymmetric fluxes and investigate the possibility for extreme vertical velocity drafts to act as a local kinetic energy injection mechanism and/or to enhance exchanges between kinetic and potential energy. Finally, we test our filtering procedure against the standard Fourier decomposition on a stably stratified flow forced at intermediate scale as well as on a HIT high-resolution DNS.

The paper is organized as follows. Sec. II briefly introduces the fluid framework under study and some of its features. Sec. III describes the space-filtered energy equations in the Boussinesq framework. Sec. IV provides an overview of the numerical framework used to perform the simulations analyzed. In Sec. V we assess the feedback of the extreme vertical velocity drafts on local energy transfer and exchanges, as it occurs in localized regions of the physical space. In Sec. VI, main results are summarized and further discussed.

II. LARGE-SCALE INTERMITTENCY IN STRATIFIED GEOPHYSICAL FLOWS

Turbulent flows develop strong field gradients, a phenomenon known as (small-scale or internal) intermittency, routinely observed in the atmosphere and the oceans, as well as in numerical simulations. These are as-

sociated with patches of dissipation distributed more or less homogeneously within the flow. However, intermittency is not only present at the smallest scales. In stratified geophysical flows, strong fluctuations of the fields are in fact observed at scales comparable to that of the mean flow [12, 13, 16, 27]. The large-scale intermittent behavior of the vertical velocity and temperature has recently been investigated in DNS of the Boussinesq equations, exploring a parameter space relevant for the atmosphere and the oceans, and allowing for the characterization of this phenomenon in terms of the interplay between internal gravity waves and turbulent motions. In particular, very large fluctuations in the vertical component of the velocity and potential temperature, diagnosed through the kurtosis of the fields, were observed at Froude numbers of order 10^{-2} [11, 20]. By examining the kurtosis of the vertical velocity (K_w), a transition was found across values of Fr of this order, as stratification strengthens, leading to heavy non-Gaussian tails of the probability distribution functions (PDFs). The existence of a resonant regime characterized by enhanced large-scale intermittency was invoked, based on a one-dimensional model proposed in Rorai *et al.* [10] and Feraco *et al.* [11], to explain the emergence of strong velocity and potential temperature field fluctuations, associated with localized overturning [31], enhanced mixing and dissipation [23–25].

III. SPACE-FILTERING APPROACH FOR STABLY STRATIFIED FLOWS: COMPUTING AXISYMMETRIC FLUXES

The rationale behind using the space-filter approach to investigate the feedback of large-scale vertical drafts on the flow fields is that the “sub-grid” scale energy transfer and exchange terms obtained from the filtered equations are proxies of the classical Fourier fluxes that can in this case be defined locally in the physical space [32], as it will be shown in the following. This approach will therefore be used to investigate the point-wise, redistribution, transfer and exchange of (or between) kinetic and potential energy modes in stratified turbulent flows. Space-filtering was first employed in the context of large-eddy simulations (LES) [33, 34] and more recently it has been successfully applied in a variety of studies to investigate the energy transfer in simulations of fluids [35] and plasmas [36–39] and also analyzing experimental data [30, 40, 41]. This work focuses on characterizing the contribution of the vertical velocity drafts to the transfer of kinetic and potential energy. Specifically, three-dimensional DNS of the Boussinesq equations, as reported below, will be analyzed:

$$\partial_t \mathbf{u} + \boldsymbol{\omega} \times \mathbf{u} = -N\theta \mathbf{e}_z - \nabla \mathcal{P} + \nu \nabla^2 \mathbf{u} + \mathbf{F}_{\text{ext}}, \quad (1)$$

$$\partial_t \theta + (\mathbf{u} \cdot \nabla) \theta = Nw + \kappa \nabla^2 \theta, \quad (2)$$

where \mathbf{u} is the velocity field (with $\nabla \cdot \mathbf{u} = 0$), θ the temperature fluctuations around a mean temperature θ_0 , $\boldsymbol{\omega} \doteq \nabla \times \mathbf{u}$ the flow vorticity, $N \doteq \sqrt{-(g/\theta_0)\partial\bar{\theta}/\partial z}$ the Brunt-Väisälä frequency, $\mathbf{g} \doteq -g\mathbf{e}_z$ the gravity, \mathcal{P} the total pressure¹, $w \doteq \mathbf{u} \cdot \mathbf{e}_z$ the component of the flow along the gravity direction, and \mathbf{F}_{ext} an external forcing applied to the velocity field. The parameters ν and κ are kinematic viscosity and diffusivity, respectively. From the Boussinesq equations (1)–(2) it is straightforward to obtain evolution equations for kinetic and potential energies, $\mathcal{E}_u \doteq |\mathbf{u}|^2/2$ and $\mathcal{E}_\theta \doteq \theta^2/2$:

$$\partial_t \mathcal{E}_u + \nabla \cdot (\mathcal{P}\mathbf{u}) = -N\theta w + D_\nu + \epsilon_{\text{ext}}, \quad (3)$$

$$\partial_t \mathcal{E}_\theta + \nabla \cdot (\mathcal{E}_\theta \mathbf{u}) = N\theta w + D_\kappa, \quad (4)$$

here the dissipation terms are $D_\nu \doteq \nu(\nabla^2 \mathcal{E}_u - \|\boldsymbol{\Sigma}\|^2)$, $\|\boldsymbol{\Sigma}\|^2 = \boldsymbol{\Sigma} : \boldsymbol{\Sigma} = \Sigma_{ij}\Sigma_{ji}$ being the square modulus of the strain tensor $\Sigma_{ij} \doteq \partial_i u_j$, and $D_\kappa \doteq \kappa(\nabla^2 \mathcal{E}_\theta - |\nabla\theta|^2)$. The external kinetic energy injection rate is $\epsilon_{\text{ext}} \doteq \mathbf{F}_{\text{ext}} \cdot \mathbf{u}$. The term $N\theta w$ that appears with opposite sign in both equations (3) and (4), often referred to as buoyancy flux B_f [11], represents a “conversion” term between the kinetic and potential energies. These two energies are coupled through the nonlinear interaction between vertical velocity and temperature fluctuations, w and θ , respectively. By performing a spatial average over the whole fluid domain (operation denoted by $\langle \dots \rangle$), assuming vanishing fluxes at the boundaries, i.e., that $\langle \nabla \cdot (\dots) \rangle = 0$, the above energy equations read as

$$\partial_t \langle \mathcal{E}_u \rangle = -\langle N\theta w \rangle + \langle D_\nu \rangle + \langle \epsilon_{\text{ext}} \rangle, \quad (5)$$

$$\partial_t \langle \mathcal{E}_\theta \rangle = \langle N\theta w \rangle + \langle D_\kappa \rangle. \quad (6)$$

The term $\langle N\theta w \rangle$ is responsible for the exchanges between the two types of energy, \mathcal{E}_u and \mathcal{E}_θ , and it disappears when summing up equations (5) and (6) to obtain an equation for the total energy $\mathcal{E}_{\text{tot}} = \mathcal{E}_u + \mathcal{E}_\theta$ (conserved in case of vanishing dissipation, $D_\nu = D_\kappa = 0$, and no external energy injection, $\langle \epsilon_{\text{ext}} \rangle = 0$).

A. Filtered energy equations

Following the approach detailed in Cerri and Camporeale [37] and references therein, we apply the space-filter technique to equations (1)–(2), deriving the evolution equations for the “large-scale filtered” kinetic and potential energies. This procedure consists in applying a low-pass filter at the cutoff scale ℓ_* and then restoring a filtered version of the energy equations, analogously

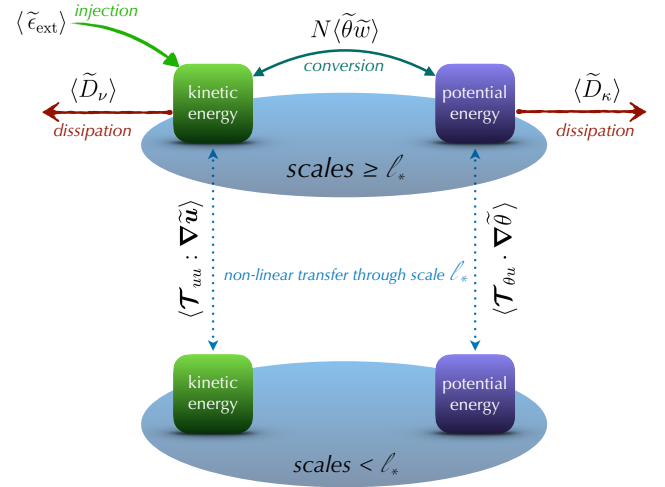


FIG. 1. Schematics of the channels resulting from the space-averaged energy equations for the filtered flux terms (14)–(15). $\ell_* \sim 1/k_*$ denotes the characteristic scale of the applied low-pass filter.

to those in (3) and (4), describing the evolution of the large-scale (i.e., $\ell \geq \ell_*$) kinetic and potential energies. The filtered terms stemming from the nonlinear terms in the Boussinesq equations will be called “sub-grid terms”, which explicitly represent the energy transfer between (all) the scales $\ell \geq \ell_*$ and (all) the scales below the filter $\ell < \ell_*$. This procedure does not assume the locality of the interactions in the Fourier space, so that the sub-grid terms account for (multiple) couplings between any of the scales smaller than ℓ_* with any of the scales larger than ℓ_* . The space-filtered version of a vector field $\mathbf{v}(\mathbf{x}, t)$ will be denoted as $\tilde{\mathbf{v}}(\mathbf{x}, t)$, and is defined as the convolution of \mathbf{v} with a filter function G :

$$\tilde{\mathbf{v}}(\mathbf{x}, t) \doteq \int_{\mathcal{V}} G(\mathbf{x} - \boldsymbol{\xi}) \mathbf{v}(\boldsymbol{\xi}, t) d^3 \boldsymbol{\xi}, \quad (7)$$

where \mathcal{V} is the entire spatial domain. The filtering operation in (7) is such that it commutes with differentiation in time and space:

$$\widetilde{\partial_t \mathbf{v}} = \partial_t \tilde{\mathbf{v}} \quad \text{and} \quad \widetilde{\nabla \cdot \mathbf{v}} = \nabla \cdot \tilde{\mathbf{v}}. \quad (8)$$

However, the convolution is a linear operator, i.e., $\widetilde{\mathbf{v}\mathbf{v}} \neq \tilde{\mathbf{v}}\tilde{\mathbf{v}}$, hence we define the corresponding “sub-grid term” as

$$\mathcal{T}_{vv} \doteq \widetilde{\mathbf{v}\mathbf{v}} - \tilde{\mathbf{v}}\tilde{\mathbf{v}}. \quad (9)$$

If ℓ_* is the cutoff scale associated with the filter (as discussed above), then \mathcal{T}_{vv} describes the coupling of all the scales $\ell \geq \ell_*$ to all the scales $\ell < \ell_*$ due to the nonlinear term $\mathbf{v}\mathbf{v}$. With the above definitions in mind, one obtains the filtered Boussinesq equations by applying the filtering procedure to equations (1)–(2) and appropriately rewriting the nonlinear terms:

¹ This scalar quantity includes the kinetic energy density (per unit mass), $|\mathbf{u}|^2/2$, as a consequence of rearranging the nonlinear term in the Navier-Stokes equation, $(\mathbf{u} \cdot \nabla)\mathbf{u} = \boldsymbol{\omega} \times \mathbf{u} + \nabla(|\mathbf{u}|^2/2)$.

$$\partial_t \tilde{\mathbf{u}} + \tilde{\boldsymbol{\omega}} \times \tilde{\mathbf{u}} + \mathcal{T}_{\boldsymbol{\omega} \times \mathbf{u}} = -N\tilde{\theta} \mathbf{e}_z - \nabla \tilde{\mathcal{P}} + \nu \nabla^2 \tilde{\mathbf{u}} + \tilde{\mathbf{F}}_{\text{ext}}, \quad (10)$$

$$\partial_t \tilde{\theta} + \nabla \cdot (\tilde{\theta} \tilde{\mathbf{u}} + \mathcal{T}_{\theta u}) = N\tilde{w} + \kappa \nabla^2 \tilde{\theta}, \quad (11)$$

where $\mathcal{T}_{\boldsymbol{\omega} \times \mathbf{u}} \doteq \widetilde{\boldsymbol{\omega} \times \mathbf{u}} - \tilde{\boldsymbol{\omega}} \times \tilde{\mathbf{u}}$ and $\mathcal{T}_{\theta u} \doteq \widetilde{\theta \mathbf{u}} - \tilde{\theta} \tilde{\mathbf{u}}$. From equations (10) and (11) one can derive the expression for the filtered kinetic and potential energy by taking the scalar product of (10) with $\tilde{\mathbf{u}}$ and multiplying (11) by $\tilde{\theta}$, that reads as ²

$$\partial_t \tilde{\mathcal{E}}_u + \nabla \cdot \left[\left(\tilde{\mathcal{P}} - \frac{\text{tr}[\mathcal{T}_{uu}]}{2} \right) \tilde{\mathbf{u}} + \mathcal{T}_{uu} \cdot \tilde{\mathbf{u}} \right] = -N\tilde{\theta} \tilde{w} + \mathcal{T}_{uu} : \nabla \tilde{\mathbf{u}} + \tilde{D}_\nu + \tilde{\epsilon}_{\text{ext}}, \quad (12)$$

$$\partial_t \tilde{\mathcal{E}}_\theta + \nabla \cdot \left(\tilde{\mathcal{E}}_\theta \tilde{\mathbf{u}} + \mathcal{T}_{\theta u} \tilde{\theta} \right) = N\tilde{\theta} \tilde{w} + \mathcal{T}_{\theta u} \cdot \nabla \tilde{\theta} + \tilde{D}_\kappa, \quad (13)$$

where $\tilde{D}_\nu \doteq \nu[\nabla^2 \tilde{\mathcal{E}}_u - \|\tilde{\boldsymbol{\Sigma}}\|^2]$, $\tilde{D}_\kappa \doteq \kappa(\nabla^2 \tilde{\mathcal{E}}_\theta - |\nabla \tilde{\theta}|^2)$, and $\tilde{\epsilon}_{\text{ext}} \doteq \tilde{\mathbf{F}}_{\text{ext}} \cdot \tilde{\mathbf{u}}$ are the filtered dissipation terms and kinetic energy injection rate in (3)–(4), respectively. In rewriting the term $\tilde{\mathbf{u}} \cdot \mathcal{T}_{\boldsymbol{\omega} \times \mathbf{u}}$ we used the incompressibility condition, $\nabla \cdot \tilde{\mathbf{u}} = 0$, along with the fact that the sub-grid term arising from $\boldsymbol{\omega} \times \mathbf{u}$ can be rewritten as $\mathcal{T}_{\boldsymbol{\omega} \times \mathbf{u}} = \nabla \cdot [\mathcal{T}_{uu} - (\text{tr}[\mathcal{T}_{uu}]/2)\mathbf{I}]$, $\mathcal{T}_{uu} \doteq \widetilde{\mathbf{u}\mathbf{u}} - \tilde{\mathbf{u}}\tilde{\mathbf{u}}$ being the sub-grid Reynolds stress tensor of the flow (while $\text{tr}[\mathcal{T}_{uu}]$ is its trace), and \mathbf{I} the identity tensor. We remind the reader that the symbol “:” is the tensor scalar product, i.e., $\mathcal{T}_{uu} : \nabla \tilde{\mathbf{u}} = (\mathcal{T}_{uu})_{ij} \partial_j \tilde{u}_i$ (for a detailed derivation of equations (12)–(13) see appendix B). Analogously to equations (5)–(6), performing volume averages of (12)–(13) leads to

$$\partial_t \langle \tilde{\mathcal{E}}_u \rangle = -N\langle \tilde{\theta} \tilde{w} \rangle - \langle \mathcal{S}_u \rangle + \langle \tilde{D}_\nu \rangle + \langle \tilde{\epsilon}_{\text{ext}} \rangle, \quad (14)$$

$$\partial_t \langle \tilde{\mathcal{E}}_\theta \rangle = N\langle \tilde{\theta} \tilde{w} \rangle - \langle \mathcal{S}_\theta \rangle + \langle \tilde{D}_\kappa \rangle, \quad (15)$$

where we defined the sub-grid terms $\mathcal{S}_u \doteq -\mathcal{T}_{uu} : \nabla \tilde{\mathbf{u}}$ and $\mathcal{S}_\theta \doteq -\mathcal{T}_{\theta u} \cdot \nabla \tilde{\theta}$ for brevity. From equation (14) one infers that the transfer rate of kinetic energy through a scale ℓ_* stems from the interaction between the strain tensor at scales $\ell \geq \ell_*$, $\tilde{\boldsymbol{\Sigma}} = \nabla \tilde{\mathbf{u}}$, and the sub-grid Reynolds stress, \mathcal{T}_{uu} . Similarly, equation (15) shows that the transfer rate of potential energy through ℓ_* depends on the interaction of the sub-grid heat flux, $\mathcal{T}_{\theta u}$, with the gradient of temperature fluctuations at scales

$\ell \geq \ell_*$, $\nabla \tilde{\theta}$. Potential and kinetic energy channels are coupled by $N \neq 0$, which allows the conversion rate between the two energy forms through the nonlinear term involving temperature and vertical fluctuations at scales $\ell \geq \ell_*$, i.e., $N\langle \tilde{\theta} \tilde{w} \rangle$. A schematic view of the global (i.e., space-averaged) dynamics of the kinetic and potential energy channels described by equations (14)–(15) is depicted in Figure 1. Summing up the equations for filtered kinetic and potential energies, one obtains the scale-by-scale conservation equation for the filtered total energy, $\tilde{\mathcal{E}}_{\text{tot}} \doteq \tilde{\mathcal{E}}_u + \tilde{\mathcal{E}}_\theta$, in which the conversion terms $N\tilde{\theta} \tilde{w}$ cancel out and the transfer rate of total energy across the scale ℓ_* is given by $\mathcal{S}_{\text{tot}} = \mathcal{S}_u + \mathcal{S}_\theta$. Finally, it is worth reminding that at any fixed ℓ_* , if a sub-grid term \mathcal{S} is positive (negative), then \mathcal{S} represents a sink (source) term as seen by the energy reservoir $\tilde{\mathcal{E}}$ at scales $\ell \geq \ell_*$, and thus the energy is being transferred to (from) scales $\ell < \ell_*$ from (to) scales $\ell \geq \ell_*$. This sign convention for the sub-grid terms is consistent with the classical Fourier energy flux (see Section IV A). In order to include the conversion between the two energy channels as possible source/sink terms for each other energy reservoir, we define the “conservative outflux” of kinetic (potential) energy from scales $\ell \geq \ell_*$ as $\Phi_u \doteq \mathcal{S}_u + N\tilde{\theta} \tilde{w}$ ($\Phi_\theta \doteq \mathcal{S}_\theta - N\tilde{\theta} \tilde{w}$); this allows a direct comparison between the volume-average sub-grid terms computed here and the scale-to-scale Fourier energy flux. Note that the conversion terms describe energy conversions occurring entirely at scales $\ell \geq \ell_*$, whereas only the sub-grid terms properly describe the energy transfer through scales, i.e., the transfer between the “scale domains” $\ell \geq \ell_*$ and $\ell < \ell_*$ that is passing through the cutoff ℓ_* (the sign of the sub-grid term giving the direction of this transfer). Given that the conversion terms cancel out for the total energy, it readily follows that $\Phi_{\text{tot}} = \mathcal{S}_{\text{tot}}$. In general, the final form of the filtered Boussinesq equations (10)–(11), hence of the corresponding filtered energy equations (14)–(15), are independent of the particular choice made for the filtering kernel G (e.g. low-pass, top-hat, Gaussian, or other filter shapes). Here we perform convolutions between the physical variables (i.e., velocity and temperature fluctuations) and the Butterworth filter, defined in the Fourier space as $G^{(n)}(k) = 1/[1 + (k/k^*)^{2n}]$, with $n = 4$ and k^* the characteristic wave number above which fluctuations are filtered out, thus corresponding to a low-pass filter. The choice of an isotropic filter acting on circular or spherical shells (defined by the wave number modulus only, k) is straightforward for the analysis of homogeneous and isotropic flows, either in two or three dimensions [28]. However, stratified turbulent flows are anisotropic and a reasonable option is to implement a spatial filters analogous to classical Fourier integrations through planes or cylindrical shells, as when the computation of parallel and perpendicular energy fluxes is operated in the Fourier space (see IV A for the definition). It will be shown in the next section how the correspondence between reduced fluxes in the Fourier space and sub-grid flux terms is achieved by modifying the symmetry properties of the

² Since the total pressure \mathcal{P} contains the contribution from the kinetic energy density, $|\mathbf{u}|^2/2$, the term $\tilde{\mathcal{P}} - \text{tr}[\mathcal{T}_{uu}]/2$ in (12) corresponds to $\tilde{p} + |\tilde{\mathbf{u}}|^2/2 = \tilde{p} + \tilde{\mathcal{E}}_u$, where p is the actual thermal pressure of the fluid. This is a consequence of the identity $\widetilde{|\mathbf{u}|^2} = |\tilde{\mathbf{u}}|^2 + \text{tr}[\mathcal{T}_{uu}]$.

Run	k_F	N	Re	Fr	R_B	n_p
I	2.5	0	6700	∞	∞	1024^3
II	20	8	97	0.128	1.59	512^3
III	2.5	8	3800	0.076	22.1	512^3

TABLE I. Relevant parameters of the DNS analyzed: k_F is the forcing wave number, N the Brunt-Väisälä frequency, Re the Reynolds number, Fr the Froude number and R_B the buoyancy Reynolds.

filtering kernel $G^{(4)}(k_{\perp,\parallel}) = 1/[1 + (k_{\perp,\parallel}/k_{\perp,\parallel}^*)^8]$. In particular, we obtain parallel and perpendicular integrated sub-grid terms, $\mathcal{S}(k_{\parallel})$ and $\mathcal{S}(k_{\perp})$, respectively, assuming the filters $G^{(4)}(k_{\parallel})$, with $k_{\parallel} = |k_z|$ (where gravity is along the parallel direction), and $G^{(4)}(k_{\perp})$, with $k_{\perp} = (k_x^2 + k_y^2)^{1/2}$. The choice to perform filters along parallel and perpendicular directions (with respect to gravity) in the physical space, is motivated as well by the fact that numerous previous studies highlighted a different behavior of the energy transfer when fluxes result from integrations along different directions in the Fourier space, in stratified [42] and rotating stratified turbulent flows [3]. On the other hand, attention must be paid in analyzing reduced energy fluxes in turbulent flows; in particular, using DNS of the Boussinesq equations reproducing the planetary atmospheres in a realistic parameter space, it has been recently shown that partial fluxes may not capture the actual energy cascade rate in geophysical flows [2].

IV. DIRECT NUMERICAL SIMULATIONS

The Boussinesq equations (1)–(2) are solved in a triply periodic cubic box of size $L_0 = 2\pi$, discretized on a uniform grid, using the highly parallelized pseudo-spectral code GHOST [43, 44]. An external random forcing acting on the velocity field only (the temperature field is not forced) continuously injects energy in an isotropic wave number shell $k_F = 2\pi/L_F$. The main governing parameters of the flow are the Reynolds number $Re = U_{\text{rms}}L/\nu$, and the Froude number $Fr = U_{\text{rms}}L_{\text{int}}/N$. Here the integral scale L_{int} is taken as the scale at which the external forcing is applied, i.e., $L_{\text{int}} = L_F$. Combining Re and Fr parameters one can define the so-called buoyancy Reynolds number $R_B = Fr^2 Re = (\ell_{Oz}/\eta)^{4/3}$, where ℓ_{Oz} is the Ozmidov scale, below which the flow recovers isotropy (see also [45]) and η is the Kolmogorov scale, at which energy is dissipated. Table I collects the relevant parameters used in three simulations analyzed in this study: one HIT (i.e., $Fr = \infty$), with resolution $n_p = 1024^3$ (run I), and two stratified turbulent simulations performed on grids of 512^3 points, varying forcing wave number. In particular, run II is forced at intermediate scales, $k_F = 20$, while kinetic energy is injected at large scale in run I and III, $k_F \approx 2.5$. Run II, char-

acterized by weaker turbulence was used to test the filters design, comparing the sub-grid transfer terms in the equations with the classical reduced fluxes computed in the Fourier space along the perpendicular (k_{\perp}) and parallel (k_{\parallel}) directions as in Marino *et al.* [3]. Run III is the same as the one thoroughly analyzed in Marino *et al.* [23], where the feedback of the extreme vertical drafts on global spectral properties and dissipation was explored. In the present work the space filtering approach allows to extend the analysis in Marino *et al.* [23] by exploring how vertical drafts affect locally in the physical space by-scale distributions and exchanges dynamics in stably stratified flows in presence of large-scale intermittency.

A. Anisotropic fluxes vs sub-grid terms

In order to better interpret the information provided by the space-filter approach, in this section we systematically compare sub-grid terms with the fluxes computed with the usual Fourier analysis over the entire domain volume. In particular, the anisotropic energy transfer can be obtained from the axisymmetric transfer function [2, 3],

$$\tau(k_{\perp}, k_{\parallel}) \doteq \int \left[\widehat{\mathbf{u}}_{\mathbf{k}} \cdot \widehat{(\mathbf{u} \cdot \nabla \mathbf{u})}_{\mathbf{k}}^* + \widehat{\theta}_{\mathbf{k}} \cdot \widehat{(\mathbf{u} \cdot \nabla \theta)}_{\mathbf{k}}^* \right] k_{\perp} d\phi + \text{c.c.} \quad (16)$$

which can be also defined in terms of spherical coordinates as $\tau(k, \Theta)$, indicating the isotropic flux; in Eq. (16), the hat $\widehat{(\dots)}_{\mathbf{k}}$ denotes the Fourier coefficient at scale \mathbf{k} , both * and c.c. stand for complex conjugate, and ϕ is the azimuthal angle (defined with respect to the x axis; the parallel direction that defines k_{\parallel} is the z axis instead). By integrating (16) over spheres, planes, and cylinders in Fourier space, we obtain respectively,

$$T(k) = \int \tau(k, \Theta) k d\Theta, \quad (17)$$

$$T(k_{\parallel}) = \int \tau(k_{\perp}, k_{\parallel}) dk_{\perp}, \quad (18)$$

$$T(k_{\perp}) = \int \tau(k_{\perp}, k_{\parallel}) dk_{\parallel}, \quad (19)$$

The integration of these fluxes leads to Eq. 20 which represents the isotropic, parallel, and perpendicular (with respect to the direction of gravity) scale-to-scale energy flux, with $k_i \in [k, k_{\perp}, k_{\parallel}]$, respectively.

$$\Pi_T(k_i) = - \int_0^{k_i} T(k'_i) dk'_i, \quad (20)$$

This comparison proposed here aims at assessing the validity of the anisotropic space-filter approach as a proxy

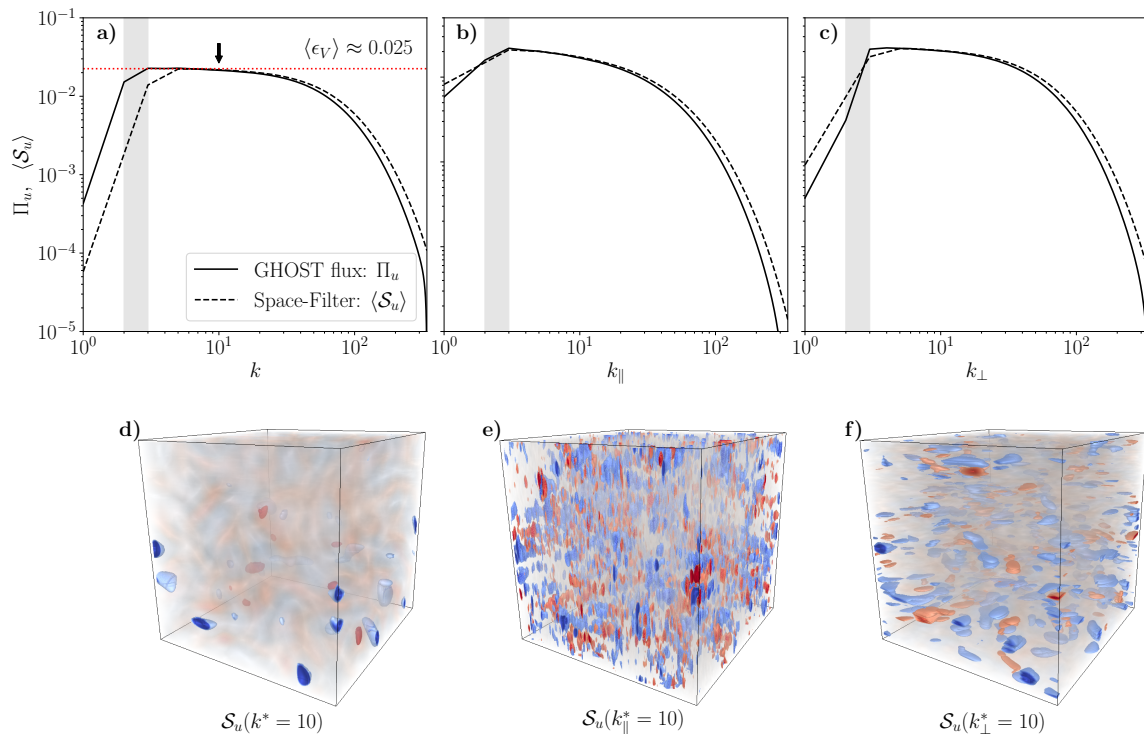


FIG. 2. Run I. Top panels: comparison between isotropic a), parallel b), and perpendicular c) volume averaged flux terms obtained from the filtered energy equations and the corresponding scale-to-scale flux obtained from global Fourier computations. The horizontal red-dotted line (panel a) indicates the volume-average kinetic dissipation rate $\langle \epsilon_V \rangle = \nu \langle (\partial_i u_j) (\partial_i u_j) \rangle$. 3D renderings of the point-wise kinetic energy sub-grid term \mathcal{S}_u in the isotropic, parallel, and perpendicular version at $k = 10$. The black arrow in panel (a) shows the cut-off scale used to produce the renderings.

for the Fourier energy flux Π_T . While Eq. (20) represents a local-in-scale energy flux through a given k^* mediated by neighboring wave numbers (i.e., a “scale-to-scale” transfer), the sub-grid terms at the same wave-number provide the global-in-scale energy flux through k^* , mediated by all the possible couplings between wave numbers with $k < k^*$ and those with $k > k^*$ (i.e., an “all-to-all” transfer). Quantitative discrepancies can therefore be interpreted as evidence of non-local transfers of energy across the scales.

Fig. 2 shows the result of the space-filter technique applied to the high resolution DNS ($n_p = 1024^3$) of a HIT flow with Reynolds number $\text{Re} = 6,700$ (run I). Left, middle and right columns refer to the application of the isotropic, parallel and perpendicular filter, respectively. The top row (panels a–c) shows the comparison between the volume-averaged kinetic energy sub-grid term $\langle \mathcal{S}_u \rangle$ (dashed black line) and the kinetic flux Π_u (solid black line); the quantities are averaged over five time steps of the simulation, covering almost one turnover time $\tau_{\text{NL}} = U_{\text{rms}}/L_{\text{int}}$ after a stationary turbulent state is reached, to obtain smooth curves and let the statistics converge. The bottom row (panels d–f) depicts three-dimensional visualizations of the kinetic energy sub-grid term \mathcal{S}_u , taken at $k^* \approx k_\eta/20$ (where k_η is the wavenumber associated to the Kolmogorov scale

η), for the isotropic (panel d), parallel (panel e) and perpendicular (panel f) filtering operation. Fig. 2 shows interesting features of the space-filter technique. The total energy flux (left panel), as well as the isotropic sub-grid term, show a forward (to small scale) energy cascade with a well-defined inertial range between $k \approx k_F$ and $k = 50 \approx k_\eta/4$. In this range, the two methods provide similar output, consistent with the volume-average dissipation rate $\langle \epsilon_V \rangle = \nu \langle (\partial_j u_i) (\partial_i u_j) \rangle$, indicated as a red dotted line. At large scale, around $k_F = 2.5$ where the forcing is applied (gray-shaded area) the discrepancy between the space filtering technique and the Fourier flux is more evident. This happens also at scales at which dissipative effects become more important, $k = 80 \approx k_\eta/2.5$, and the space filtering approach seems to systematically overestimate the energy flux. The parallel and perpendicular sub-grid terms (panels b and c) show results consistent with what was previously concluded for the isotropic flux. The same validation test was performed using a stably stratified flow simulation. Run II has been performed at 512^3 resolution with a rather low Reynolds number, due to the relatively small size of the box and the fact that energy is injected at $k_F = 20$ (see Tab. I). The spectral transfer in a simulation with parameters similar to run II, with the same forcing mechanism, has been analyzed in Marino *et al.* [3], where the different com-

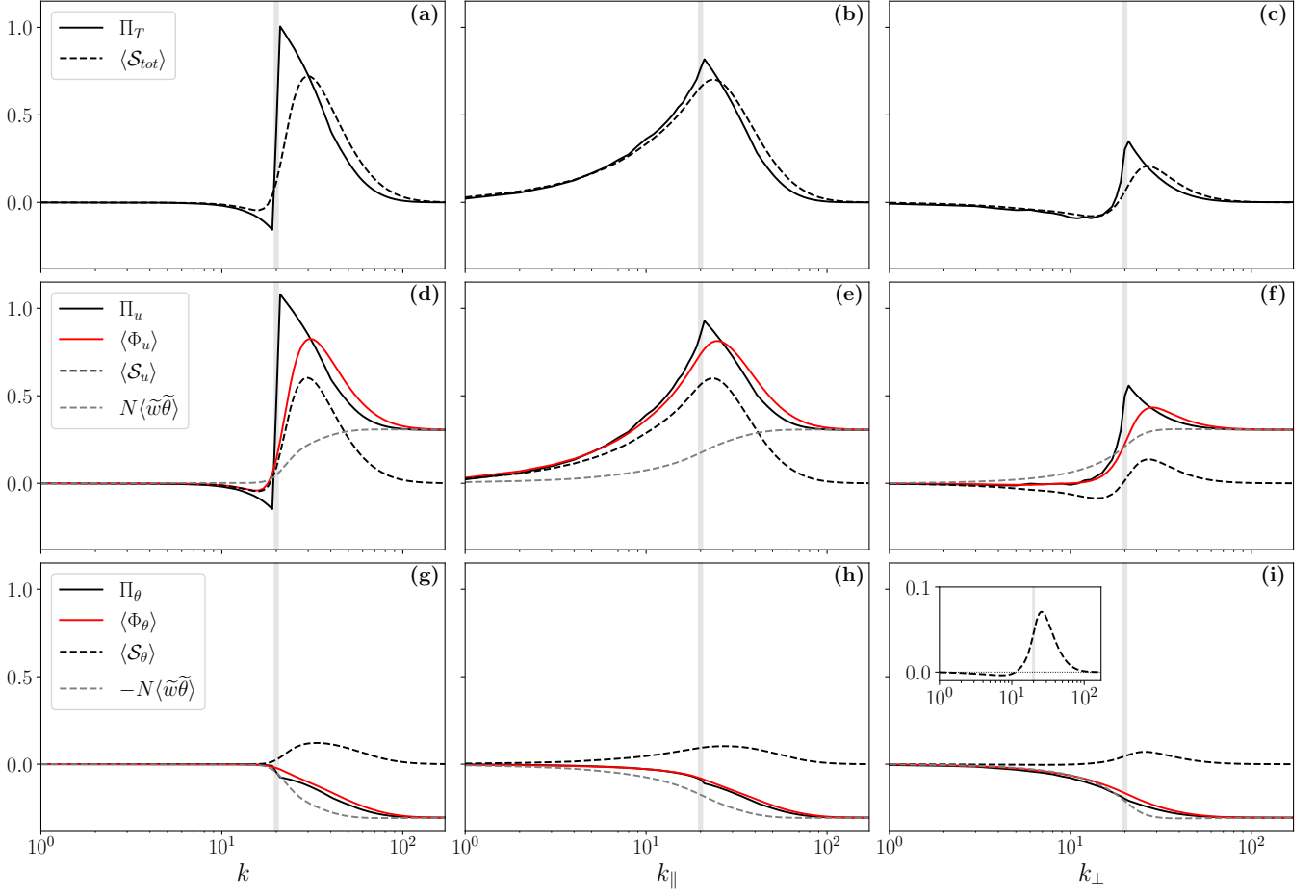


FIG. 3. Panels (a)–(c): comparison between isotropic (left), parallel (center) and perpendicular (right) scale-to-scale Fourier total energy flux Π_{tot} (black solid lines) and the total energy sub-grid flux terms (black dashed lines) for run II. In panels (d)–(f) and (g)–(i) the same comparison is proposed for the kinetic and potential energy fluxes, respectively, and the individual flux terms. For the single energy channels, $\tilde{\Phi}$ (red lines) is the sum of the cross-scale term $\langle \mathcal{S}_{u,\theta} \rangle$ and $\mp N \langle \tilde{\theta} \tilde{w} \rangle$, representing the conservative terms on the right-hand side of Eqs. (14)–(15). The channel-conversion terms alone $\mp N \langle \tilde{\theta} \tilde{w} \rangle$ are also shown (gray dashed lines). The inset in panel (i) shows a detail of the potential energy sub-grid term. A vertical dashed area denoting $k_F = 20$ is provided.

ponents of the energy transfer (isotropic, perpendicular and parallel) have been characterized showing a different behavior in presence of gravity and/or rotation. The results presented in Marino *et al.* [3] show that in this particular setup the isotropic flux $\Pi_T(k)$ is almost zero for $k < k_F$, indicating that almost no energy goes across spheres (in Fourier space) toward small wave numbers in purely stratified turbulent flows. On the other hand, the parallel flux $\Pi_T(k_{\parallel})$ is positive and dominant for all wave numbers, indicating a strong transfer toward smaller vertical scales. Completely different is the behavior of the perpendicular component of the flux $\Pi_T(k_{\perp})$ showing a range with negative values for $k < k_F$, indicating an inverse energy transfer (to large scale), and a positive flux for $k > k_F$. Here, we want to check whether this peculiar behavior can be captured by our implementation of the space-filter approach. The comparison between the two techniques is reported in Fig. 3. In panels (a)–(c)

we show the total transfer computed with the Fourier method $\Pi_T(k_i)$ (Eq. (20), solid black line) and with the sub-grid terms $\langle \mathcal{S}_{tot} \rangle = \langle \mathcal{S}_u + \mathcal{S}_{\theta} \rangle$ (black dashed line). Panels (d)–(f) and (g)–(i) show the energy flux associated with a single energy channel, i.e., kinetic (middle row) and potential (bottom row), respectively. For the latter cases, the Fourier flux (black line) is compared with the sum of the conservative terms on the right-hand side of Eqs. (14)–(15), i.e., $\tilde{\Phi}_u = \mathcal{S}_u + N\tilde{\theta}\tilde{w}$ and $\tilde{\Phi}_{\theta} = \mathcal{S}_{\theta} - N\tilde{\theta}\tilde{w}$, respectively (red lines). However, we also highlight the trend of the single terms composing the conservative flux i.e., $\mathcal{S}_{u,\theta}$ (black dashed line) and $N\tilde{\theta}\tilde{w}$ (gray dashed lines). From all the panels in Fig. 3 is evident the good agreement between the two approaches, both at large and small scales and for all the components. The discrepancy is more significant around the forcing wavenumber k_F for the intrinsic difference between the

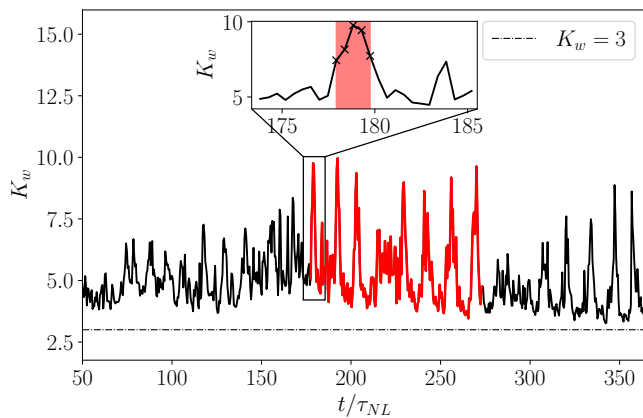


FIG. 4. Temporal evolution of kurtosis K_w of the vertical velocity run III. The red portion of the curve corresponds to the interval analyzed in Sec. VC, the red shaded area is instead analyzed in Sec. V and corresponds to $\sim 2\tau_{NL}$; the same interval is evidenced in the inset. The horizontal black dash-dotted line is the Gaussian reference value for the kurtosis $K_w = 3$.

space-filtering approach and the Fourier analysis. For $k > k_F$ the energy fluxes always indicate a downscale transfer of total energy, panels (a)–(c), with a modulation of the intensity going from the isotropic to the perpendicular component of the total energy flux. By looking at the perpendicular transfers, panel (c), the behavior previously described in terms of total Fourier energy flux is correctly recovered with the space filtering technique, showing an inverse transfer at scale $k_\perp < k_F$ and a direct transfer in the range $k_\perp > k_F$, with an inversion point with almost zero net flux at $k_\perp \sim k_F$. Such a good agreement is also obtained for the single energy channels, in panels (f) and (i). In this case, some interesting features emerge from the analysis with the space filtering approach, in particular the role of the conversion term $N\langle\tilde{\theta}\tilde{w}\rangle$ (dashed gray line in panels (d)–(i)), indicating the conversion from kinetic to potential energy if positive and vice-versa if negative, at scales $k < k_*$. Indeed, we can see from panel (f), for instance, how this term becomes the dominant contribution to the perpendicular flux at $k_\perp \gtrsim 70$, where $\langle\Phi_u\rangle \approx N\langle\tilde{\theta}\tilde{w}\rangle$: this means that kinetic energy is almost totally converted into potential at small scales (let us remind that when $N\langle\tilde{\theta}\tilde{w}\rangle$ is positive, it represents a sink term for $\langle\tilde{\mathcal{E}}_u\rangle$ and a source term for $\langle\tilde{\mathcal{E}}_\theta\rangle$ (cf. Eqs. (14)–(15)), and this likely explains why we observe an upscale potential energy flux Π_θ at any $k > k_F$. This is also consistent with the fact that the flux of total energy, both computed as $\langle S_{tot}\rangle$ or as Π_T , goes to zero at small scales, i.e. there is no net cascade toward smaller scales in that range, but just a small-scale kinetic-to-potential energy conversion (plus dissipation—not shown here). By looking at the potential energy transfer rate, panel (i), with the space filtering analysis we can see that the negative values, in this case,

do not indicate an inverse transfer of potential energy in the whole range of wave numbers. In fact, since for the potential energy channel there is no external forcing, this channel is only fed by the conversion of kinetic energy $\langle\Phi_\theta\rangle \approx N\langle\tilde{\theta}\tilde{w}\rangle$ at each scale. The transfer of potential energy mediated by the nonlinear term $\langle S_\theta\rangle$, in fact, still exhibits simultaneously positive (direct transfer) and negative (inverse transfer) values, although in this case the inversion scale – i.e., the scale at which $\langle S_\theta\rangle$ changes sign – is not exactly at k_F , but at slightly larger scales (around $k_\perp \approx 10$, see inset in Fig. 3). The behavior of the potential energy transfer for the three components, panels (g)–(i), is pretty much the same, with an almost zero flux at $k < k_F$ and a negative transfer dominated by the conversion term at scale $k > k_F$.

V. LOCAL ENERGY TRANSFER AND EXCHANGES TRIGGERED BY VERTICAL DRAFTS

In this section we expand the results presented in Marino *et al.* [3], showing how extreme vertical drafts developing in DNS of stratified turbulent flows [10, 11] and observed in geophysical flows [12, 15, 16] are able to generate local turbulence, enhancing kinetic and potential energy dissipation. Leveraging the space filtering approach, here we assess the feedback of the vertical drafts on the energy transfer and the kinetic-potential energy exchanges locally in the physical space. To this end, we consider only Run III (see Table I), whose parameters have been identified in [11, 20] as those associated with the highest level of large-scale intermittency of both velocity and potential temperature fields, assessed through their kurtoses, K_w and K_θ respectively. A detail of the temporal profile of K_w for Run III is presented in Fig. 4, in which the red portion of the curve identifies the time interval analyzed in Sec. VC and the inset highlights five snapshots of the simulation around a peak of kurtosis used for the following analysis. Fig. 5 shows three-dimensional renderings of the filtered fields at $t \simeq 178.8\tau_{NL}$ (see inset in Fig. 4), a time characterized by a surge of vertical drafts: panel (a) highlights the values of vertical velocity field w larger than four standard deviations ($|w/\sigma_w| > 4$), in red if positive and blue if negative; the total sub-grid energy transfer \mathcal{S}_{tot} , computed at the cutoff scale $k = 7 \approx k_B = N/U$ (the latter being the wave number associated with the buoyancy scale) for both parallel and perpendicular integrations of the filter, is presented in panels (b) and (c). Five temporal snapshots between $t = 177.9\tau_{NL}$ and $t = 179.7\tau_{NL}$, have been used to compute the flux terms, corresponding to the red-shaded area in the inset of Fig. 4. Positive values (red), being significantly more numerous and intense for the perpendicular filter, thus as a function of k_\perp , indicate a net transfer of the energy to the smaller scales. Conversely, $\mathcal{S}_{tot}(k_\parallel)$ (panel b) shows almost the same density of structures transferring energy at scales

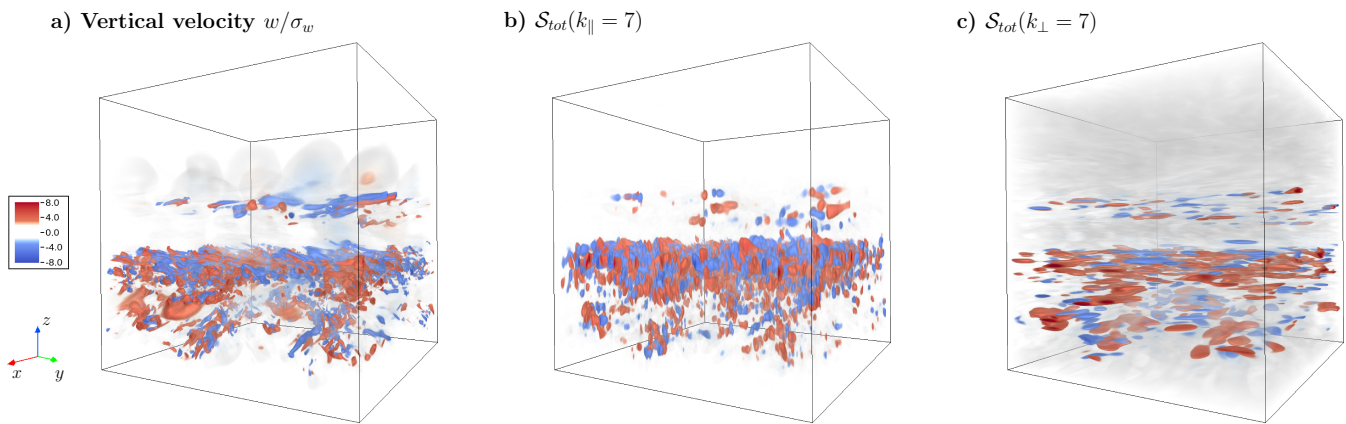


FIG. 5. Values larger than four standard deviations are highlighted in red (positive) and blue (negative) for the vertical velocity field w (panel a), and the point-wise total energy flux term, vertically filtered at $k_{\parallel} = 7$, (panel b), and the same term horizontally filtered at the perpendicular wave number k_{\perp} (panel c). For panels b) and c) positive/negative values mean downscale/upscale energy transfer.

larger (red) and smaller (blue) than the filtering scale, i.e. $\approx k_B$. Indeed, we will see more quantitatively in the following that around such a scale the net parallel energy transfer almost vanishes $\langle \mathcal{S}_{tot}(k_{\parallel} \approx k_B) \rangle \sim 0$, that interestingly is related to the typical width of the layers. In some regions of the simulation domain, there is a very good correlation between the sub-grid term and the extreme values of the vertical velocity.

$ w/\sigma_w $	[0, 2.5)	[2.5, 3)	[3, 4)	[4, 6)	[6, ∞)
% volume	97.92	0.802	0.704	0.436	0.138

TABLE II. Percentage of volume occupied by points having standardized vertical velocity $|w/\sigma_w|$ in a given interval of values. The data are obtained by averaging over the five binaries shown in the inset in Fig. 4.

In order to quantitatively assess the possibility that the extreme vertical drafts may act as local energy injection mechanism in stratified turbulent flows, we perform averages of all the sub-grid terms (i.e. kinetic, potential and buoyancy flux) in sub-domains of the simulation box $N = 512^3$. In particular, at each time of the simulation the space is partitioned in terms of standardized values of the vertical velocity $|w/\sigma_w|$, then statistical bins are created to accumulate values from $|w/\sigma_w| < 2.5$ (corresponding to the domain points with vertical velocities within the Gaussian core of the distribution, accounting for $\sim 97\%$ of the total volume, to $|w/\sigma_w| \in [2.5, 3)$, $|w/\sigma_w| \in [3, 4)$, $|w/\sigma_w| \in [4, 6)$, and finally $|w/\sigma_w| \geq 6$, corresponding to portions of the domain volume characterized by the strongest vertical drafts along the temporal evolution of the simulations. As a reference, values with $|w/\sigma_w| \geq 4$ corresponds to events occurring on average on $\sim 0.6\%$ of the volume under study (see Tab. II). Number and extension of the vertical velocity bins are constrained by the necessity to have convergent statistics in each bin, at least at the lowest orders (i.e., mean

and standard deviation).

A. Perpendicular cross-scale energy transfer

In Fig. 6 we report panels showing the nonlinear transfer through scales of the various energy channels averaged over different sub-domains identified by increasing intervals of the standardized vertical velocity $|w/\sigma_w|$ (see legend), and obtained using the perpendicular k_{\perp} filtering kernel. Panels (a), (b), and (c) show the kinetic $\langle \mathcal{S}_u \rangle$, potential $\langle \mathcal{S}_{\theta} \rangle$ and total energy flux $\langle \mathcal{S}_{tot} \rangle$, respectively, while panel (d) represent the kinetic-to-potential conversion term (or buoyancy flux) $N \langle \tilde{\theta} \tilde{w} \rangle$; the two bottom panels show instead the conservative fluxes of kinetic (e) and potential energy (f), proportional in the inertial range to the energy transfer rate, where the dissipation and the large-scale forcing are negligible (see (14) and (15)). Generally, for all the quantities, higher energy transfer is associated on average with larger values of $|w/\sigma_w|$, at all the scales. The local transfer rate associated with the extreme events (assuming as a reference those are characterized by $|w/\sigma_w| > 4$) is on average up to ten times larger than the volume-averaged energy transfer rate for both the kinetic and potential energy channels, i.e. $\langle \varepsilon_V \rangle \approx 0.288$ and $\langle \varepsilon_{\theta} \rangle \approx 0.024$. The cross-scale flux computed over regions with $|w/\sigma_w| < 2.5$ (black curve in Fig. 6) shows a peak of transfer close to the forcing shell $k_F \approx 2.5$, as it is expected for a continuously forced simulation. By looking at the total energy transfer Fig. 6 (c) one infers that the forward transfer (i.e., toward smaller scales) is stronger over a wide range of intermediate perpendicular scales, $k_F \lesssim k_{\perp} \lesssim 40$ ($k_{Oz} \approx 42$ being the Ozmidov scale estimated over the same time interval), in the regions of the domain where the vertical velocity is higher. The total energy transfer seems also dominated by the kinetic energy contribution, showing

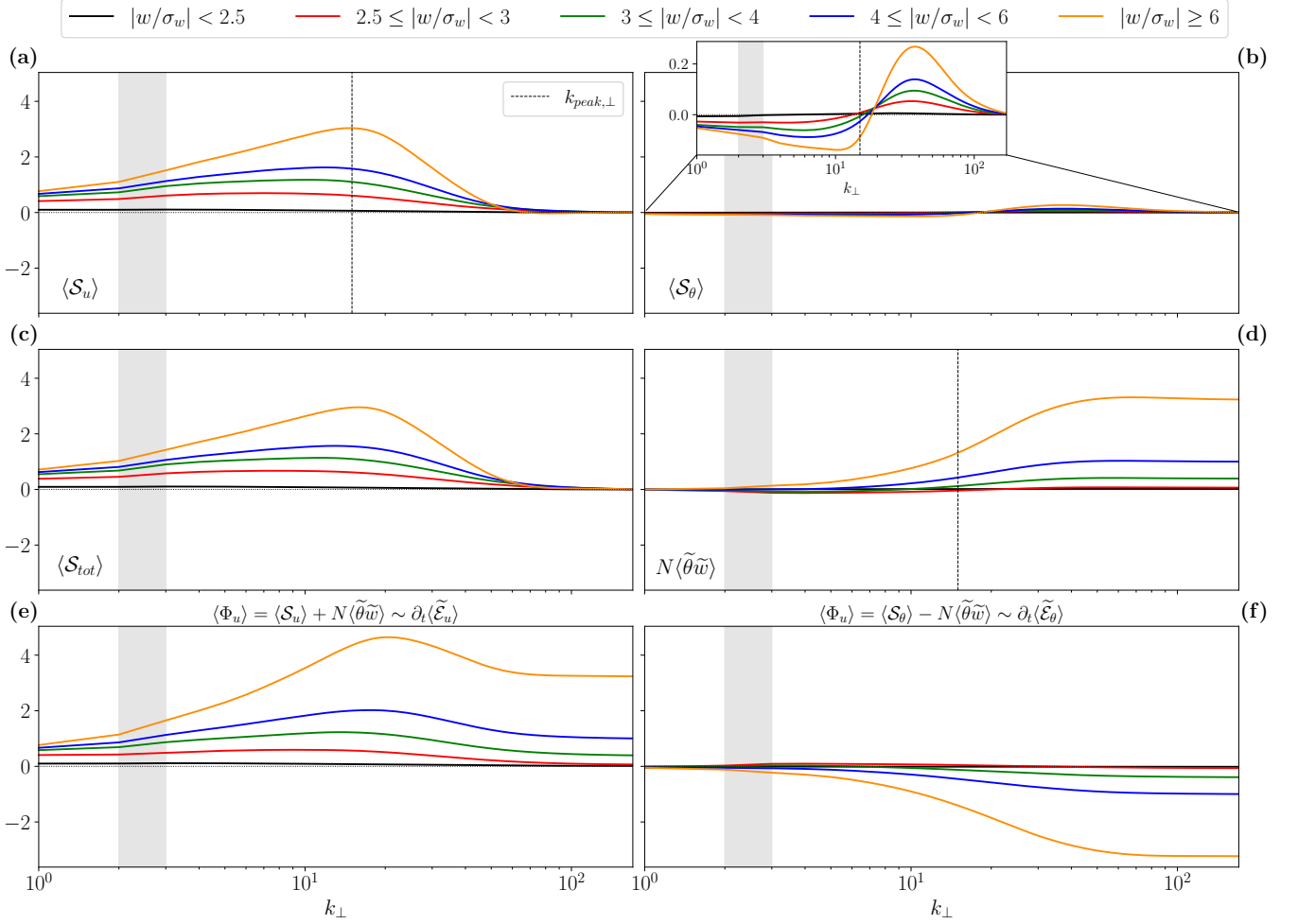


FIG. 6. Kinetic (a), potential (b), total energy flux terms (c), and buoyancy flux (d) as a function of the filtering wave number $k_\perp = \sqrt{k_x^2 + k_y^2}$ for the axisymmetric version of the filtering kernel applied to run III. The gray shaded area indicates the shell where kinetic energy is injected $k_F = [2, 3]$ in the simulation through the external forcing. The vertical dashed lines (in panels b, c, and d), at $k_{peak,\perp} = 15 \approx 2k_B$, indicate where the maximal coupling between velocity and potential temperature fields occurs. Panels (e) and (f) show the sum of the previous terms for each energy channel, being proportional to the energy flux $\partial_t \langle \tilde{\mathcal{E}}_{u,\theta} \rangle$ in the inertial range, where the dissipation terms $\langle \mathcal{D}_{\nu,\kappa} \rangle$ are negligible.

the same features and trend (Fig. 6, panel a). There is as well a significant conversion from kinetic to potential energy, approximately over the same range of scales, again proportionally to values of $|w/\sigma_w|$ (Fig. 6, panel d). At scale $k_\perp \lesssim 10$ the energy conversion is negligible and less sensitive to $|w/\sigma_w|$, while at intermediate scales, $k_B \lesssim k_\perp \lesssim k_{Oz}$, the filtered buoyancy flux $N \langle \tilde{\theta} \tilde{w} \rangle$ increases more rapidly the larger the vertical velocity. Beyond $k_\perp \approx k_{Oz}$, the kinetic-to-potential conversion saturates, meaning that there is no significant exchange between these two energy channels at smaller scales. Nevertheless, we mention that $N \langle \tilde{\theta} \tilde{w} \rangle$ slightly decreases at $k_\perp \gtrsim k_{Oz}$, though it is difficult to appreciate from the figure, which means that a small portion of the potential energy is converted back into kinetic energy at the smallest scales, especially for high values of $|w/\sigma_w|$. Looking at the potential energy flux term in Fig. 6(b), an

interesting phenomenon is observed: a bi-directional potential energy transfer, simultaneously direct (at scales $k_\perp \gtrsim 20$) and inverse (at scales $k_\perp \lesssim 10$) seems to be associated with the emergence of strong vertical velocity draft, strengthening the higher the values of the vertical velocity. The wave number at which the sign of the energy transfer switches is close to $k_{peak,\perp} \approx 15$ (vertical dashed lines in panels b, c, and d of Fig. 6), the scale at which the energy conversion from kinetic to potential is maximal ($d \langle \tilde{\theta} \tilde{w} \rangle / dk$), roughly equal to twice the buoyancy wave number ($k_B = N/U \approx 7$). This is also the scale at which the peak values of kinetic and total energy transfer are attained (at least in the high vertical velocity bins, $|w/\sigma_w| \geq 4$), as shown in Fig. 6 (a,c). Another length scale that could be associated with the emergence of the bi-directional potential energy flux, representing the maximum vertical distance that can be covered by

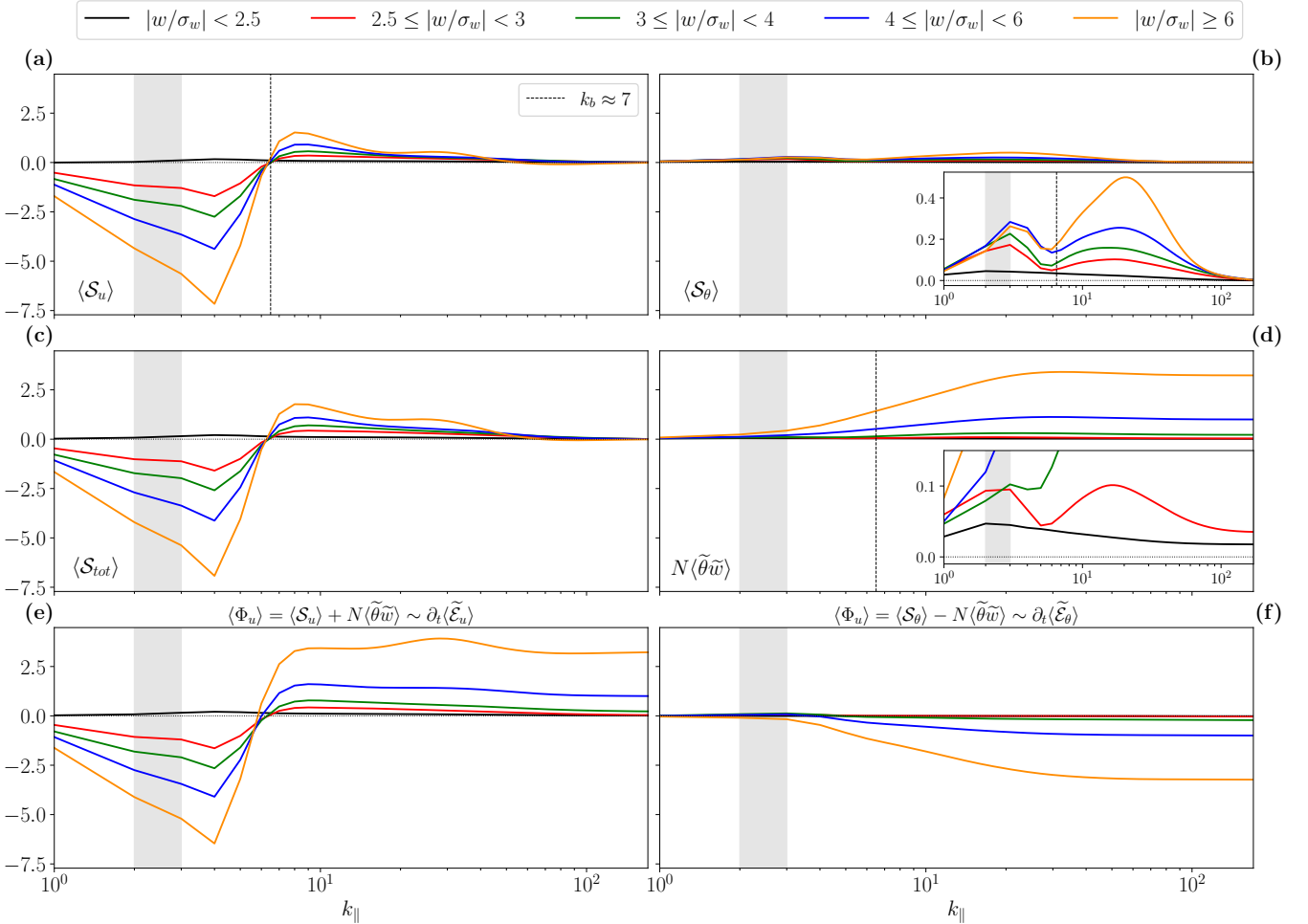


FIG. 7. Same as Fig. 6 for the vertically filtered quantity, here shown as a function of parallel wave numbers $k_{\parallel} = |k_z|$. The vertical dashed lines (panels b and c) indicate the buoyancy wave number k_B .

a fluid parcel before returning to its equilibrium position, is the Ellison scale $\ell_{\text{Eil}} = 2\pi\theta_{\text{rms}}/N$. For run III, $k_{\text{Eil}} \approx 17$ which approximately corresponds to the potential flux inversion scale. The scenario stemming from this analysis is that – consistently with the findings in Marino *et al.* [23] – powerful vertical velocity drafts emerging in a parameter space compatible with geophysical flows [11] would boost at certain locations of the simulation domain (at intermediate scales) the direct energy transfer already powered by the external large-scale velocity field forcing; on the other hand, through the coupling term $N\tilde{\theta}\tilde{w}$, the potential-energy conversion would act as a forcing mechanism to the temperature field (not externally forced), triggering a simultaneous transfer of potential energy to both large and small scales (as shown by $\langle \mathcal{S}_\theta \rangle$). This bi-directional transfer is proportional to the intensity of the vertical drafts, vanishing in the bin corresponding to values $|w/\sigma_w| < 2.5$.

B. Parallel cross-scale energy transfer

Analogously to what was done in the previous section, here we investigate the energy transfer through the sub-grid terms obtained by the application of the filtering kernel depending on the vertical wave numbers $k_{\parallel} = |k_z|$ only. Even in this case the filter is applied point-wise in the real space, then averages of the energy fluxes are computed over the same sub-domains and time interval. The results are summarized in Fig. 7. The behavior of the various sub-grid terms is significantly different. The different energy channels (i.e., kinetic, potential, and total) in panels (a), (b), and (c), respectively, together with the energy conversion term (panel d), show three distinct regimes. For $k_{\parallel} \ll k_B$, with $k_B \sim N/U \approx 7$ (vertical dashed lines in panels (b) and (d) of Fig. 7), energy is converted from kinetic to potential, on average, for $|w/\sigma_w| < 4$, while the opposite happens for regions characterized by the strongest vertical drafts, $|w/\sigma_w| > 4$ (see inset in panel d). Indeed, the decreasing trend for $k_{\parallel} > k_F$ indicates that part of the energy, initially in-

jected by the forcing into the velocity field and converted into potential temperature fluctuations by the buoyancy term, is then being transferred from potential to kinetic in the inertial range until this process saturates at small-scales. At these scales, for values for $|w/\sigma_w| > 2.5$ the total and kinetic energy fluxes (panels a and c) are negative, indicating that energy is transferred to the large scales. A direct transfer – though much weaker – is instead detected for values belonging to sub-regions corresponding to the bin $|w/\sigma_w| < 2.5$. The wave number at which the direction of the transfer inverts coincides quite accurately with the buoyancy scale $k_B = N/U$. In the same range a local minimum of the cross-scale potential energy transfer occurs (see inset in panel b of Fig. 7), likely related to the fact that part of the potential energy is converted into kinetic energy around this scale. For $k_B < k_{\parallel} \lesssim k_{Oz}$, on average the energy is converted from kinetic to potential in the entire domain. This range is characterized by a downscale (direct) transfer of kinetic and potential energy, proportional to the magnitude of the vertical velocity, as already observed for k_{\perp} . Finally, for $k_{\parallel} \gtrsim k_{Oz}$, the direct flux of total and kinetic energy persists, but the conversion is again reversed showing a net but weak flux from potential to kinetic energy. The observed behavior of the energy conversion term around the buoyancy scale is in agreement with other numerical studies analyzing Eulerian fields in space [10, 46–49], as well as Lagrangian velocities and temperatures in the physical space [50].

C. Temporal evolution of the cross-scale energy transfer

In this section more than one hundred turnover times of run III are analyzed, corresponding to the red portion of the vertical velocity kurtosis K_w in Fig. 4. The oscillating behavior of K_w , with values as high as $K_w \approx 10$ and troughs close to the Gaussian reference (see Fig. 4) was characterized in Marino *et al.* [23] by postulating a fast evolution of the system between two slow manifolds (one associated with waves, the other with the overturning eddy instabilities). In Fig. 8 we report the temporal variation of the volume-averaged sub-grid terms (within the range from $k_{\parallel} > k_F$ to $k_{\parallel} \approx k_{\eta}$) for the two sub-regions corresponding to $|w/\sigma_w| < 3$ and $|w/\sigma_w| > 5$, left and right panels respectively. For sake of visibility, the palettes of left panels emphasize values nearly ten times smaller than those of the right panels. In panel (a), the temporal variation of K_w appears as a black dashed line. As it was observed for the power spectral density [23], which is a second-order quantity, even the energy fluxes – thus a third-order quantity – averaged over the entire domain (let us recall that points with $|w/\sigma_w| < 3$ represent roughly the 98.7% of the volume) show a temporal modulation that correlates with the evolution in time of the kurtosis K_w . This further corroborates the evidence presented in [11, 20, 23], that extreme verti-

cal drafts do globally stir the flow, generating local turbulence, enhancing small-scale, dissipation mixing and intermittency. By comparing the effect of drafts on regions with $|w/\sigma_w| < 3$ and with $|w/\sigma_w| > 5$ in Fig. 8, there is a substantial difference in terms of typical spatial scales, intensity, and overall features. Indeed, for the total and kinetic energy transfers (panels a–d), the regions characterized by vertical drafts are characterized by a bi-directional energy flux, as observed in the previous section, with an inversion scale that is slightly modulated by the intensity of extreme events. The cross-scale potential energy flux is largely positive at any k_{\parallel} for both regions, with or without extreme events, panels (e) and (f) respectively. However, also in this case substantial differences exist in terms of intensity and scale at which the maximum transfer occurs. For $|w/\sigma_w| < 3$ (panel e), the maximum of $\langle \mathcal{S}_{\theta} \rangle$ always falls at a scale close to the forcing shell k_F , as expected, whereas the intensity directly correlates with the vertical velocity kurtosis. On the other hand, in regions with $|w/\sigma_w| > 5$ (panel f), the average potential energy transfer rate is pretty constant over the entire time interval, but the scale of the maximum strongly varies with the emergence of extreme events. The kinetic-to-potential exchanges mediated by $N\tilde{\theta}\tilde{w}$, shown in panels (g) and (h), reflect the persistence of the typical features observed in the previous section. As expected, the most efficient conversion of energy for $|w/\sigma_w| < 3$ (panel g) occurs close to the forcing scales; indeed since the runs analyzed are all driven by kinetic energy injection only, the potential temperature fluctuations (null at $t = 0$) are energized by the coupling between the two fields, which is maximal at large-scale. The other regions show instead energy conversion peaks in the same range of scales where the the feedback of the vertical drafts is more prominent, i.e. $k_{\parallel} \gtrsim k_B$, with a strong variation related to K_w . This temporal analysis helps further elucidating the role of the velocity in driving the temperature field in the simulations under study, that is enhanced by the emergence of extreme vertical drafts.

VI. CONCLUSIONS

In a certain range of Froude numbers, stratified flows were found to develop in DNS large-scale intermittency, in the form of strong vertical velocity drafts and sudden surges in potential temperature [10, 11, 20]. These events, observed in geophysical flows [12, 13, 15, 16], are considered extreme as they are characterized by intensities that are several standard deviations larger than their reference average scalar values. Emerging randomly in space and time, generating local turbulence and enhancing dissipation [23], they make the flow inhomogeneous, requiring appropriate methodologies to assess their feedback on the energy transfer in the circumscribed regions of the domain where they are detected. Here, we employed the space-filtering (or coarse-graining) technique

PARALLEL FILTER

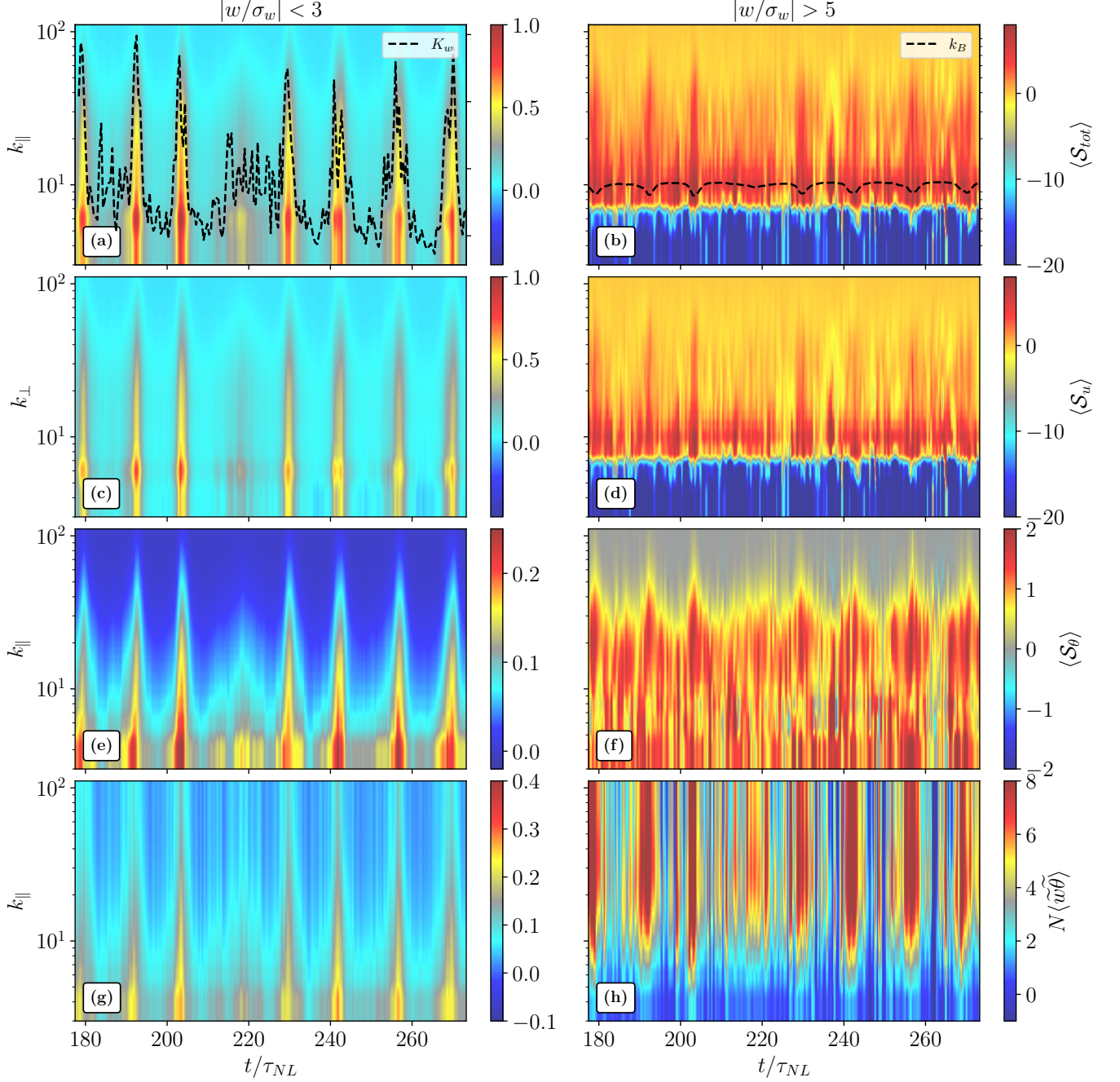


FIG. 8. Cross-scale transfer along $k_{\parallel} = |k_z|$ of total, (a)–(b), kinetic, (c)–(d), and potential energy (e)–(f), as well as the energy conversion term in panels (g)–(h). The left panels show averages computed on regions with $|w/\sigma_w| < 3$, the right panels for $|w/\sigma_w| > 5$. The black dashed line in panel (a) is the temporal profile of the vertical velocity kurtosis K_w , reported for the entire integration time in Fig. 4, the dashed line in panel (b) is a dissipation-based buoyancy wave number $k_B = N/(\varepsilon_V L)^{1/3}$. Colors in the left panels correspond to values nearly ten times smaller than those in right panels.

to explore the dynamics of stratified flows characterized by large-scale extreme events. Widely utilized in the literature to analyze neutral [29, 30, 40] as well as electrically conductive [28, 38, 39, 51–53] turbulent flows, the space filtering approach proved to be a reliable proxy of

the classical Fourier flux (which is global-in-space) capable of providing local-in-space information on energy transfers and exchanges across the scales. In this work, the standard space filtering procedure was refined and adapted to the Boussinesq framework and its associated

energy equations; then, integrations of the flux terms over cylindrical and planar filtering manifolds have been compared with parallel ($k_{\parallel} = |k_z|$) and perpendicular ($k_{\perp} = \sqrt{k_x^2 + k_y^2}$) energy fluxes computed in the Fourier space, as done for instance in Marino *et al.* [3] and Alexakis and Chibbaro [54]. This test demonstrated the excellent agreement between classical (global) Fourier fluxes and estimates of the energy transfer obtained through the space filtering by averaging flux terms over the whole domain in HIT and stratified flows forced either at large or intermediate scales. The space filtering approach was then implemented on a stably stratified DNS characterized by $Fr \approx 0.08$, a value that was shown to be strongly intermittent up to hundreds of turnover times [20, 23], producing the following outcomes:

1. The space filtering analysis revealed that, in regions where powerful vertical velocity drafts develop, enhanced forward kinetic energy transfers are observed at large-intermediate scales – peaking at scale which is roughly half the buoyancy scale $L_B \sim 1/k_B$ of the system – due to the coupling between the “sub-grid” (or, “turbulent”) Reynolds stress tensor \mathcal{T}_{uu} and the large-scale strain tensor $\nabla \tilde{\mathbf{u}}$.
2. In the analyzed simulation, where no external forcing was applied to the (potential) temperature field, vertical velocity drafts act as a mechanism for locally converting energy from kinetic to potential, both along the vertical and horizontal directions in the spectral space; this conversion is mediated by the buoyancy nonlinearity $N\langle\theta w\rangle$ that couples velocity and temperature fields in the Boussinesq framework. Interestingly, this process seems driving a dual transfer of potential energy, simultaneously toward both large and small scales, in the perpendicular direction (k_{\perp}) roughly within the turbulent inertial range. Such a behavior is evidenced by the change of sign of $\langle\mathcal{S}_{\theta}\rangle$ around $k_{\perp} \sim 20$, approximately corresponding to the maximum of energy conversion rate from kinetic to potential, as observed through $N\tilde{\theta}\tilde{w}$. These exchanges, quantified here in terms of filtered buoyancy flux, $N\tilde{\theta}\tilde{w}$, may also affect the mixing properties of the flow, inducing local variations of the buoyancy flux.
3. Along the parallel direction in Fourier space (k_{\parallel}), a bi-directional total energy transfer, developing around the buoyancy scale $k_B = N/U \approx 7$, is associated with the strongest vertical velocity drafts ($|w/\sigma_w| > 2.5$). For $k < k_B$ the total energy flux appears indeed to be negative (corresponding to an upscale transfer) and almost twice as intense as the forward energy transfer, occurring at $k > k_B$. These regimes can be explained in terms of different coupling between the velocity and temperature fields. At scales larger than k_B , energy conversion associated with regions of strong vertical drafts

is, on average, predominantly from potential to kinetic; on the other hand, within the inertial range, the scenario is compatible with what is observed for the perpendicular energy flux.

The evidence that stratified flows, in a certain region of the parameter space compatible with the atmosphere and the oceans, develop strong large-scale intermittent events in the velocity and temperature fields, being able of mediating energy transfers and conversion (as shown in Marino *et al.* [23]), may suggest potential improvements of the parametrization in weather and climate models. Among the physical processes that we plan to include in future extensions of the present study there is certainly rotation, which is critical to describe the dynamics of the Earth’s atmosphere at large scales and of the oceans. Considering extra terms in the equations would come, of course, with an additional computational cost since, in the presence of forcing, simultaneous direct and inverse energy cascades develop when the Rossby number ($Ro = U_{\text{rms}}/[fL_{\text{int}}]$) is small enough [2, 6–8]. The space filtering procedure that we proposed here is well-suited for applications to the case of rotating and stratified fluids, as well as to other intermittent, transient, and non-homogeneous turbulent flows observed in nature and in laboratories.

ACKNOWLEDGMENTS

R.F. and R.M. acknowledge support from the project “EVENTFUL” (ANR-20-CE30-0011), funded by the French “Agence Nationale de la Recherche” - ANR through the program AAPG-2020. S.S.C. is supported by the French government through the UCA^{JEDI} Investments in the Future project managed by the National Research Agency (ANR) with the reference number ANR-15-IDEX-0001 and by the ANR grant “MiCRO” with the reference number ANR-23-CE31-0016. E.C. was partially supported by NASA grants 80NSSC20K1580 “Ensemble Learning for Accurate and Reliable Uncertainty Quantification” and 80NSSC20K1275 “Global Evolution and Local Dynamics of the Kinetic Solar Wind”. The computing resources utilized in this work were provided by PMCS2I at the École Centrale de Lyon. The authors are grateful to Annick Pouquet for the useful discussions had during her visit at the École Centrale de Lyon, in may-june 2024.

Appendix A: Boussinesq equations for a stratified, rotating fluid

The starting equations for the incompressible fluid-velocity field, \mathbf{u} with $\nabla \cdot \mathbf{u} = 0$, and the temperature

fluctuations, θ , in the Boussinesq approximation are

$$\frac{\partial \mathbf{u}}{\partial t} + \boldsymbol{\omega} \times \mathbf{u} + 2\boldsymbol{\Omega} \times \mathbf{u} = -N\theta \mathbf{e}_z - \nabla \mathcal{P} + \nu \nabla^2 \mathbf{u}, \quad (\text{A1})$$

$$\frac{\partial \theta}{\partial t} + (\mathbf{u} \cdot \nabla) \theta = Nw + \kappa \nabla^2 \theta, \quad (\text{A2})$$

where $\boldsymbol{\omega} \doteq \nabla \times \mathbf{u}$ is the flow vorticity, $\boldsymbol{\Omega}$ is the rotation rate of the system, $N \doteq \sqrt{-(g/\theta_0)\partial\bar{\theta}/\partial z}$ is the stratification parameter of the background fluid due to the gravity acceleration $\mathbf{g} = -g\mathbf{e}_z$, $\mathcal{P} = p/\rho_0 + |\mathbf{u}|^2/2 = \theta + |\mathbf{u}|^2/2$ is the total pressure³ (per unit mass), and $w \doteq \mathbf{u} \cdot \mathbf{e}_z$ is the component of the flow along the stratification direction (here taken to be along z). The parameters ν and κ are the kinematic viscosity and the diffusivity, respectively.

1. Energy equation of the system

Here, we derive the evolution equations for the energy of the flow, $\mathcal{E}_u \doteq |\mathbf{u}|^2/2$, and for the ‘‘potential’’ energy, $\mathcal{E}_\theta \doteq \theta^2/2$. We anticipate that, in the incompressible limit, these two channels can exchange energy only when a non-vanishing stratification is present (i.e., through the parameter N) due to the interactions between vertical flows and temperature fluctuations, via a term $N\theta w$.

a. Energy equation of the fluid-flow field

By taking the scalar product of equation (A1) with \mathbf{u} , and making use of the incompressibility condition $\nabla \cdot \mathbf{u} = 0$, one obtains the following energy equation:

$$\frac{\partial \mathcal{E}_u}{\partial t} + \nabla \cdot (\mathcal{P}\mathbf{u}) = -N\theta w + \nu[\nabla^2 \mathcal{E}_u - \|\boldsymbol{\Sigma}\|^2], \quad (\text{A3})$$

where $\|\boldsymbol{\Sigma}\|^2 = \boldsymbol{\Sigma} : \boldsymbol{\Sigma} = \Sigma_{ij}\Sigma_{ji}$ is the square modulus of the strain tensor $\Sigma_{ij} \doteq \partial_i u_j$.

b. Potential-energy equation

Analogously, by multiplying equation (A2) by θ , one obtains the evolution equation for the potential energy:

$$\frac{\partial \mathcal{E}_\theta}{\partial t} + \nabla \cdot (\mathcal{E}_\theta \mathbf{u}) = N\theta w + \kappa[\nabla^2 \mathcal{E}_\theta - |\nabla \theta|^2]. \quad (\text{A4})$$

2. Summary of the energy channels and equation for the total energy

Gathering together the two equations above, one has the system describing the two energy channels \mathcal{E}_u and \mathcal{E}_θ ,

$$\frac{\partial \mathcal{E}_u}{\partial t} + \nabla \cdot [(\mathcal{E}_u + \theta)\mathbf{u}] = -N\theta w + D_\nu, \quad (\text{A5})$$

$$\frac{\partial \mathcal{E}_\theta}{\partial t} + \nabla \cdot (\mathcal{E}_\theta \mathbf{u}) = N\theta w + D_\kappa, \quad (\text{A6})$$

where we have defined $D_\nu \doteq \nu[\nabla^2 \mathcal{E}_u - \|\boldsymbol{\Sigma}\|^2]$ and $D_\kappa \doteq \kappa[\nabla^2 \mathcal{E}_\theta - |\nabla \theta|^2]$ for shortness. If averaged over the entire spatial domain under consideration, denoted by $\langle \dots \rangle$, and assuming vanishing fluxes at the boundaries (i.e., $\langle \nabla \cdot (\dots) \rangle = 0$), the above equations read as

$$\frac{\partial \langle \mathcal{E}_u \rangle}{\partial t} = -\langle N\theta w \rangle + \langle D_\nu \rangle, \quad (\text{A7})$$

$$\frac{\partial \langle \mathcal{E}_\theta \rangle}{\partial t} = \langle N\theta w \rangle + \langle D_\kappa \rangle. \quad (\text{A8})$$

From the above equations, it is clear that the term $\langle N\theta w \rangle$ is responsible for the energy flow between the two channels, \mathcal{E}_u and \mathcal{E}_θ .

Summing up equations (A5)–(A6), one obtains the evolution equation for the total energy, $\mathcal{E} = \mathcal{E}_u + \mathcal{E}_\theta$:

$$\frac{\partial \mathcal{E}}{\partial t} + \nabla \cdot [(\mathcal{E} + \theta)\mathbf{u}] = D_\nu + D_\kappa. \quad (\text{A9})$$

Appendix B: Filtered version of the Boussinesq equations

We now apply the filtering procedure to equations (A1)–(A2). After rewriting the nonlinear terms as the nonlinearity of the filtered quantities plus a sub-grid term, one obtains

$$\begin{aligned} \frac{\partial \tilde{\mathbf{u}}}{\partial t} + \tilde{\boldsymbol{\omega}} \times \tilde{\mathbf{u}} + \mathcal{T}_{\times u}^{(\omega)} + 2(\tilde{\boldsymbol{\Omega}} \times \tilde{\mathbf{u}} + \mathcal{T}_{\times u}^{(\Omega)}) = \\ -(\tilde{N}\tilde{\theta} + \mathcal{T}_N^{(\theta)})\mathbf{e}_z - \nabla \tilde{\mathcal{P}} + \nu \nabla^2 \tilde{\mathbf{u}}, \end{aligned} \quad (\text{B1})$$

$$\frac{\partial \tilde{\theta}}{\partial t} + \nabla \cdot (\tilde{\theta} \tilde{\mathbf{u}} + \mathcal{T}_{\theta u}) = \tilde{N}\tilde{w} + \mathcal{T}_N^{(w)} + \kappa \nabla^2 \tilde{\theta}, \quad (\text{B2})$$

where we have introduced the following sub-grid terms:

$$\mathcal{T}_{\times u}^{(v)} \doteq \widetilde{\mathbf{v} \times \mathbf{u}} - \tilde{\mathbf{v}} \times \tilde{\mathbf{u}}, \quad (\text{B3})$$

$$\mathcal{T}_{\theta u} \doteq \widetilde{\theta \mathbf{u}} - \tilde{\theta} \tilde{\mathbf{u}}, \quad (\text{B4})$$

³ This scalar includes the term $|\mathbf{u}|^2/2$ as a consequence of rewriting the nonlinear term that would usually appear in the Navier-Stokes equation by using the vector identity $(\mathbf{u} \cdot \nabla)\mathbf{u} = \boldsymbol{\omega} \times \mathbf{u} + \nabla(|\mathbf{u}|^2/2)$

and,

$$\mathcal{T}_N^{(F)} \doteq \widetilde{N}\widetilde{F} - \widetilde{N}\widetilde{F}, \quad (\text{B5})$$

with $\mathcal{T}_N^{(\dots)} = 0$ for constant, homogeneous stratification, $N = N_0 = \text{cst}$, and, analogously, $\mathcal{T}_{\times u}^{(\Omega)} = 0$ for rigid, solid-body rotation, $\boldsymbol{\Omega} = \Omega_0 \mathbf{e}_z$ with $\Omega_0 = \text{cst}$.

In deriving the filtered version of the energy equations, it is important to explicitly rewrite the filtered total pressure, $\widetilde{\mathcal{P}}$, since it contains sub-grid terms. In fact, it is easy to see that

$$\widetilde{\mathcal{P}} = \widetilde{\theta} + \frac{|\widetilde{\mathbf{u}}|^2}{2} = \widetilde{\theta} + \frac{|\widetilde{\mathbf{u}}|^2}{2} + \frac{1}{2}\mathcal{T}_{u^2}, \quad (\text{B6})$$

with

$$\mathcal{T}_{u^2} \doteq \widetilde{\mathbf{u}} \cdot \widetilde{\mathbf{u}} - \widetilde{\mathbf{u}} \cdot \widetilde{\mathbf{u}} = \text{tr}[\mathcal{T}_{uu}], \quad (\text{B7})$$

where $\mathcal{T}_{uu} \doteq \widetilde{\mathbf{u}}\widetilde{\mathbf{u}} - \widetilde{\mathbf{u}}\widetilde{\mathbf{u}}$ is the sub-grid (or ‘‘turbulent’’) Reynolds stress tensor of the flow (or, written by components, $\mathcal{T}_{uu;ij} = \widetilde{u}_i\widetilde{u}_j - \widetilde{u}_i\widetilde{u}_j$).

1. Equation for the filtered flow energy

By taking the scalar product of equation (B1) with $\widetilde{\mathbf{u}}$ and rewriting some terms, one obtains the evolution equation for the filtered flow energy, $\widetilde{\mathcal{E}}_u \doteq |\widetilde{\mathbf{u}}|^2/2$:

$$\begin{aligned} \frac{\partial \widetilde{\mathcal{E}}_u}{\partial t} + \nabla \cdot (\widetilde{\mathcal{P}}\widetilde{\mathbf{u}}) &= -\widetilde{N}\widetilde{\theta}\widetilde{w} + \nu[\nabla^2 \widetilde{\mathcal{E}}_u - \|\widetilde{\boldsymbol{\Sigma}}\|^2] \\ &\quad - \widetilde{\mathbf{u}} \cdot (\mathcal{T}_{\times u}^{(\omega)} + 2\mathcal{T}_{\times u}^{(\Omega)}) - \widetilde{w}\mathcal{T}_N^{(\theta)}, \end{aligned} \quad (\text{B8})$$

where $\widetilde{\boldsymbol{\Sigma}}_{ij} = \partial_i \widetilde{u}_j$ is the strain tensor associated with the flow velocity at scales $> \ell$, $\widetilde{\mathbf{u}}$. The terms on the right-hand side of (B8) that involve sub-grid quantities are the terms that determine the transfer of flow energy through scale ℓ . Note that $\mathcal{T}_{\times u}^{(\omega)}$ can be rewritten in terms of the sub-grid Reynolds stress tensor of the flow, \mathcal{T}_{uu} , as $\mathcal{T}_{\times u}^{(\omega)} = \nabla \cdot (\mathcal{T}_{uu} - \text{tr}[\mathcal{T}_{uu}]\mathbf{I})/2$. Therefore, $\widetilde{\mathbf{u}} \cdot \mathcal{T}_{\times u}^{(\omega)}$ is in effect related the energy transfer through scale ℓ that arises because of the interaction between the strain tensor at scales $> \ell$, $\widetilde{\boldsymbol{\Sigma}} = \nabla \widetilde{\mathbf{u}}$, and the ‘‘turbulent’’ Reynolds stress tensor \mathcal{T}_{uu} ,

$$\widetilde{\mathbf{u}} \cdot \mathcal{T}_{\times u}^{(\omega)} = \nabla \cdot \left[\left(\mathcal{T}_{uu} - \frac{\text{tr}[\mathcal{T}_{uu}]}{2} \mathbf{I} \right) \cdot \widetilde{\mathbf{u}} \right] - \mathcal{T}_{uu} : \widetilde{\boldsymbol{\Sigma}}, \quad (\text{B9})$$

where in the last step we have used the incompressibility condition, $\nabla \cdot \widetilde{\mathbf{u}} = 0$. As a result, equation (B8) can be rewritten as

$$\begin{aligned} \frac{\partial \widetilde{\mathcal{E}}_u}{\partial t} + \nabla \cdot \left[(\widetilde{\mathcal{E}}_u + \widetilde{\theta}) \widetilde{\mathbf{u}} + \mathcal{T}_{uu} \cdot \widetilde{\mathbf{u}} \right] &= -\widetilde{N}\widetilde{\theta}\widetilde{w} \\ &\quad + \nu[\nabla^2 \widetilde{\mathcal{E}}_u - \|\widetilde{\boldsymbol{\Sigma}}\|^2] + \mathcal{T}_{uu} : \widetilde{\boldsymbol{\Sigma}} - 2\widetilde{\mathbf{u}} \cdot \mathcal{T}_{\times u}^{(\Omega)} - \widetilde{w}\mathcal{T}_N^{(\theta)}, \end{aligned} \quad (\text{B10})$$

where the symbol ‘‘:’’ means tensor scalar product, i.e., $\mathcal{T}_{uu} : \widetilde{\boldsymbol{\Sigma}} = \mathcal{T}_{ij}\widetilde{\boldsymbol{\Sigma}}_{ji}$.

2. Equation for the filtered potential energy

Multiplying equation (B2) by $\widetilde{\theta}$, after rewriting some terms, provides the evolution equation for the filtered potential energy, $\widetilde{\mathcal{E}}_\theta \doteq |\widetilde{\theta}|^2/2$:

$$\frac{\partial \widetilde{\mathcal{E}}_\theta}{\partial t} + \nabla \cdot (\widetilde{\mathcal{E}}_\theta \widetilde{\mathbf{u}}) = \widetilde{N}\widetilde{\theta}\widetilde{w} + \kappa[\nabla^2 \widetilde{\mathcal{E}}_\theta - |\nabla \widetilde{\theta}|^2] - \widetilde{\theta}(\nabla \cdot \mathcal{T}_{\theta u}) + \widetilde{\theta}\mathcal{T}_N^{(w)}, \quad (\text{B11})$$

where now the sub-grid term $\mathcal{T}_{\theta u}$ plays the role of a sort of ‘‘turbulent’’ heat-flux vector for the temperature fluctuations $\widetilde{\theta}$ at scales $> \ell$.

3. Summary of the filtered energy equations and equation for the filtered total energy

Gathering equations (B10) and (B11), and rewriting some terms in the latter, one has the filtered version of the system of equations (A5)–(A6):

$$\begin{aligned} \frac{\partial \widetilde{\mathcal{E}}_u}{\partial t} + \nabla \cdot \left[(\widetilde{\mathcal{E}}_u + \widetilde{\theta}) \widetilde{\mathbf{u}} + \mathcal{T}_{uu} \cdot \widetilde{\mathbf{u}} \right] &= -\widetilde{N}\widetilde{\theta}\widetilde{w} + \widetilde{D}_\nu \\ &\quad + \mathcal{T}_{uu} : \widetilde{\boldsymbol{\Sigma}} - 2\widetilde{\mathbf{u}} \cdot \mathcal{T}_{\times u}^{(\Omega)} - \widetilde{w}\mathcal{T}_N^{(\theta)}, \end{aligned} \quad (\text{B12})$$

$$\begin{aligned} \frac{\partial \widetilde{\mathcal{E}}_\theta}{\partial t} + \nabla \cdot (\widetilde{\mathcal{E}}_\theta \widetilde{\mathbf{u}} + \mathcal{T}_{\theta u} \widetilde{\theta}) &= \widetilde{N}\widetilde{\theta}\widetilde{w} + \widetilde{D}_\kappa \\ &\quad + \mathcal{T}_{\theta u} \cdot \nabla \widetilde{\theta} + \widetilde{\theta}\mathcal{T}_N^{(w)}, \end{aligned} \quad (\text{B13})$$

which, when space averaged, reduce to

$$\begin{aligned} \frac{\partial \langle \widetilde{\mathcal{E}}_u \rangle}{\partial t} &= -\langle \widetilde{N}\widetilde{\theta}\widetilde{w} \rangle + \langle \widetilde{D}_\nu \rangle \\ &\quad + \langle \mathcal{T}_{uu} : \widetilde{\boldsymbol{\Sigma}} \rangle - \langle 2\widetilde{\mathbf{u}} \cdot \mathcal{T}_{\times u}^{(\Omega)} \rangle - \langle \widetilde{w}\mathcal{T}_N^{(\theta)} \rangle, \end{aligned} \quad (\text{B14})$$

$$\frac{\partial \langle \widetilde{\mathcal{E}}_\theta \rangle}{\partial t} = \langle \widetilde{N}\widetilde{\theta}\widetilde{w} \rangle + \langle \widetilde{D}_\kappa \rangle + \langle \mathcal{T}_{\theta u} \cdot \nabla \widetilde{\theta} \rangle + \langle \widetilde{\theta}\mathcal{T}_N^{(w)} \rangle, \quad (\text{B15})$$

or, for the simple case of constant stratification and rigid rotation,

$$\frac{\partial \langle \widetilde{\mathcal{E}}_u \rangle}{\partial t} = -N_0 \langle \widetilde{\theta}\widetilde{w} \rangle + \langle \widetilde{D}_\nu \rangle + \langle \mathcal{T}_{uu} : \nabla \widetilde{\mathbf{u}} \rangle, \quad (\text{B16})$$

$$\frac{\partial \langle \widetilde{\mathcal{E}}_\theta \rangle}{\partial t} = N_0 \langle \widetilde{\theta}\widetilde{w} \rangle + \langle \widetilde{D}_\kappa \rangle + \langle \mathcal{T}_{\theta u} \cdot \nabla \widetilde{\theta} \rangle. \quad (\text{B17})$$

It is clear from the above equations that:

1. The stratification is the only ingredient that connects the two energy channels, which would be otherwise independent from each other. The terms

$\langle \mathcal{T}_{uu} : \nabla \tilde{\mathbf{u}} \rangle$ and $\mathcal{T}_{\theta u} \cdot \nabla \tilde{\theta}$ indeed provide the energy transfer through scale of the standard hydrodynamic case.

2. A non-uniform stratification and/or a non-uniform rotation can strongly modify the energy transfer through scales of a single channel via the terms $\mathcal{T}_N^{(\theta)}$, $\mathcal{T}_N^{(w)}$, and $\mathcal{T}_{\times u}^{(\Omega)}$, as well as the energy exchange between $\tilde{\mathcal{E}}_u$ and $\tilde{\mathcal{E}}_\theta$ (since $\langle \tilde{N} \tilde{\theta} \tilde{w} \rangle \neq N_0 \langle \tilde{\theta} \tilde{w} \rangle$).

The equation for the filtered total energy, $\tilde{\mathcal{E}} = \tilde{\mathcal{E}}_u +$

$\tilde{\mathcal{E}}_\theta$, is obtained by summing up the two energy equations (B12)–(B13):

$$\frac{\partial \tilde{\mathcal{E}}}{\partial t} + \nabla \cdot \left[\left(\tilde{\mathcal{E}} + \tilde{\theta} \right) \tilde{\mathbf{u}} + \mathcal{T}_{uu} \cdot \tilde{\mathbf{u}} + \mathcal{T}_{\theta u} \tilde{\theta} \right] = \tilde{D}_\nu + \tilde{D}_\kappa + \mathcal{S}_{\text{sg}}, \quad (\text{B18})$$

where the sub-grid term \mathcal{S}_{sg} for the total energy is

$$\mathcal{S}_{\text{sg}} = \mathcal{T}_{uu} : \nabla \tilde{\mathbf{u}} + \mathcal{T}_{\theta u} \cdot \nabla \tilde{\theta} - 2 \tilde{\mathbf{u}} \cdot \mathcal{T}_{\times u}^{(\Omega)} - \tilde{w} \mathcal{T}_N^{(\theta)} + \tilde{\theta} \mathcal{T}_N^{(w)}, \quad (\text{B19})$$

where the symbol “:” means a tensor scalar product, i.e., $\mathcal{T}_{uu} : \nabla \tilde{\mathbf{u}} = \mathcal{T}_{ij} \partial_j \tilde{u}_i$.

-
- [1] J. P. Laval, J. C. McWilliams, and B. Dubrulle, *Phys. Rev. E* **68**, 036308 (2003), arXiv:physics/0304080 [physics.flu-dyn].
 - [2] A. Alexakis, R. Marino, P. D. Mininni, A. van Kan, R. Foldes, and F. Feraco, *Science* **383**, 1005 (2024).
 - [3] R. Marino, P. D. Mininni, D. L. Rosenberg, and A. Pouquet, *Phys. Rev. E* **90**, 023018 (2014), arXiv:1407.4580 [physics.flu-dyn].
 - [4] E. Lindborg, *Journal of Fluid Mechanics* **550**, 207 (2006).
 - [5] R. Marino, P. D. Mininni, D. Rosenberg, and A. Pouquet, *EPL (Europhysics Letters)* **102**, 44006 (2013).
 - [6] A. Pouquet and R. Marino, *Phys. Rev. Lett.* **111**, 234501 (2013).
 - [7] R. Marino, A. Pouquet, and D. Rosenberg, *Phys. Rev. Lett.* **114**, 114504 (2015).
 - [8] D. Balwada, J.-H. Xie, R. Marino, and F. Feraco, *Science Advances* **8**, eabq2566 (2022).
 - [9] P. Billant and J.-M. Chomaz, *Journal of Fluid Mechanics* **418**, 167 (2000).
 - [10] C. Rorai, P. D. Mininni, and A. Pouquet, *Phys. Rev. E* **89**, 043002 (2014), arXiv:1308.6564 [physics.flu-dyn].
 - [11] F. Feraco, R. Marino, A. Pumir, L. Primavera, P. D. Mininni, A. Pouquet, and D. Rosenberg, *Europhysics Letters* **123**, 44002 (2018).
 - [12] L. Mahrt, *Journal of the Atmospheric Sciences* **46**, 79 (1989).
 - [13] R. Lyu, F. Hu, L. Liu, J. Xu, and X. Cheng, *Advances in Atmospheric Sciences* **35**, 1265 (2018).
 - [14] P. Rodriguez Imazio, A. Dörnbrack, R. D. Urzua, N. Rivaben, and A. Godoy, *Journal of Geophysical Research (Atmospheres)* **127**, e2021JD035908 (2022).
 - [15] J. L. Chau, R. Marino, F. Feraco, J. M. Urco, G. Baumgarten, F. J. Lübken, W. K. Hocking, C. Schult, T. Renkowitz, and R. Lattek, *Geophysical Research Letters* **48**, e94918 (2021).
 - [16] E. A. D’Asaro, R.-C. Lien, and F. Henyey, *Journal of Physical Oceanography* **37**, 1956 (2007).
 - [17] L. F. Burlaga, *Journal of Geophysical Research* **96**, 5847 (1991).
 - [18] L. Sorriso-Valvo, R. Marino, L. Lijoi, S. Perri, and V. Carbone, *The Astrophysical Journal* **807**, 86 (2015).
 - [19] A. N. Kolmogorov, *Journal of Fluid Mechanics* **13**, 82–85 (1962).
 - [20] F. Feraco, R. Marino, L. Primavera, A. Pumir, P. D. Mininni, D. Rosenberg, A. Pouquet, R. Foldes, E. Lévêque, E. Camporeale, S. S. Cerri, H. Charuvil Asokan, J. L. Chau, J. P. Bertoglio, P. Salizzoni, and M. Marro, *EPL (Europhysics Letters)* **135**, 14001 (2021), arXiv:2106.07574 [physics.flu-dyn].
 - [21] N. E. Sujovolsky, G. B. Mindlin, and P. D. Mininni, *Phys. Rev. Fluids* **4**, 052402 (2019).
 - [22] N. E. Sujovolsky and P. D. Mininni, *Phys. Rev. Fluids* **5**, 064802 (2020).
 - [23] R. Marino, F. Feraco, L. Primavera, A. Pumir, A. Pouquet, D. Rosenberg, and P. D. Mininni, *Physical Review Fluids* **7**, 033801 (2022), arXiv:2106.15219 [physics.flu-dyn].
 - [24] A. Pouquet, D. Rosenberg, R. Marino, and C. Herbert, *Journal of Fluid Mechanics* **844**, 519–545 (2018).
 - [25] A. Pouquet, D. Rosenberg, and R. Marino, *Physics of Fluids* **31**, 105116 (2019).
 - [26] B. Pearson and B. Fox-Kemper, *Phys. Rev. Lett.* **120**, 094501 (2018).
 - [27] J. Isern-Fontanet and A. Turiel, *Journal of Physical Oceanography* **51**, 2639 (2021).
 - [28] E. Camporeale, L. Sorriso-Valvo, F. Califano, and A. Retinò, *Phys. Rev. Lett.* **120**, 125101 (2018), arXiv:1711.00291 [physics.plasm-ph].
 - [29] H. Aluie, M. Hecht, and G. K. Vallis, *Journal of Physical Oceanography* **48**, 225 (2018), arXiv:1710.07963 [physics.flu-dyn].
 - [30] M. Buziccotti, B. A. Storer, S. M. Griffies, and H. Aluie, *Earth and Space Science Open Archive*, 58 (2021).
 - [31] A. Pouquet, D. Rosenberg, R. Marino, and P. Mininni, *Atmosphere* **14**, 10.3390/atmos14091375 (2023).
 - [32] H. Aluie and S. Kurien, *EPL (Europhysics Letters)* **96**, 44006 (2011).
 - [33] M. Germano, *Journal of Fluid Mechanics* **238**, 325 (1992).
 - [34] C. Meneveau and J. Katz, *Annual Review of Fluid Mechanics* **32**, 1 (2000).
 - [35] P. Hellinger, A. Verdini, S. Landi, E. Papini, L. Franci, and L. Matteini, *Physical Review Fluids* **6**, 044607 (2021), arXiv:2103.12005 [physics.flu-dyn].
 - [36] Y. Yang, W. H. Matthaeus, T. N. Parashar, C. C. Haggerty, V. Roytershteyn, W. Daughton, M. Wan, Y. Shi, and S. Chen, *Physics of Plasmas* **24**, 072306 (2017), arXiv:1705.02054 [physics.plasm-ph].
 - [37] S. S. Cerri and E. Camporeale, *Physics of Plasmas* **27**, 082102 (2020), arXiv:2005.03130 [physics.plasm-ph].
 - [38] D. Manzini, F. Sahraoui, F. Califano, and R. Ferrand, *Phys. Rev. E* **106**, 035202 (2022), arXiv:2203.01050

- [physics.plasm-ph].
- [39] D. Manzini, F. Sahraoui, and F. Califano, *Phys. Rev. Lett.* **130**, 205201 (2023), arXiv:2208.00855 [physics.plasm-ph].
- [40] A. De Leo and A. Stocchino, *Geophysical Research Letters* **49**, e2022GL098043 (2022).
- [41] H. Khatri, S. Griffies, B. Storer, M. Buzzicotti, H. Aluie, M. Sonnewald, R. Dussin, and A. Shao, *Journal of Advances in Modeling Earth Systems* **16** (2024).
- [42] P. Billant and J.-M. Chomaz, *Physics of Fluids* **13**, 1645 (2001).
- [43] P. D. Mininni, D. Rosenberg, R. Reddy, and A. Pouquet, *Parallel Computing* **37**, 316 (2011).
- [44] D. Rosenberg, P. D. Mininni, R. Reddy, and A. Pouquet, *Atmosphere* **11**, 10.3390/atmos11020178 (2020).
- [45] T. M. Dillon, *Journal of Geophysical Research: Oceans* **87**, 9601 (1982).
- [46] G. Holloway, *Dynamics of Atmospheres and Oceans* **12**, 107 (1988).
- [47] C. Staquet and F. S. Godeferd, *Journal of Fluid Mechanics* **360**, 295–340 (1998).
- [48] G. F. Carnevale, M. Briscolini, and P. Orlandi, *Journal of Fluid Mechanics* **427**, 205–239 (2001).
- [49] G. Brethouwer, P. Billant, E. Lindborg, and J.-M. Chomaz, *Journal of Fluid Mechanics* **585**, 343–368 (2007).
- [50] S. Gallon, A. Sozza, F. Feraco, R. Marino, and A. Pumir, *Phys. Rev. Lett.* **133**, 024101 (2024), arXiv:2401.14779 [physics.flu-dyn].
- [51] Y. Yang, W. H. Matthaeus, Y. Shi, M. Wan, and S. Chen, *Physics of Fluids* **29**, 035105 (2017).
- [52] Y. Yang, M. Wan, W. H. Matthaeus, L. Sorriso-Valvo, T. N. Parashar, Q. Lu, Y. Shi, and S. Chen, *Mon. Not. Royal Astron. Soc.* **482**, 4933 (2019).
- [53] R. Foldes, S. S. Cerri, R. Marino, and E. Camporeale, *Phys. Rev. E* **110**, 055207 (2024).
- [54] A. Alexakis and S. Chibbaro, *Phys. Rev. Fluids* **5**, 094604 (2020).